The landward and seaward mechanisms of fine-sediment transport across intertidal flats in the shallow-water region – A numerical investigation

Tian-Jian Hsu[1], Shih-Nan Chen[2,*], Andrea S. Ogston[3]

[1]Center for Applied Coastal Research, Civil and Environmental Engineering, University of Delaware, Newark, DE 19716, USA

[2]Applied Ocean Physics and Engineering, Woods Hole Oceanographic Institution, Woods Hole, MA 02543, USA

[3]School of Oceanography, University of Washington, Seattle, WA 98195, USA

*Now at Institute of Oceanography, National Taiwan University, Taipei, Taiwan

ABSTRACT

This study investigates transport of fine sediment across idealized intertidal flats with emphasis on resolving processes at the tidal edge, which is defined as the very shallow region of the land-water interface. We first utilize a two-dimensional, vertical numerical model solving the non-hydrostatic Reynolds-averaged Navier-Stokes equations with a k-ε turbulence closure. The numerical model adopts the Volume of Fluid method to simulate the wetting and drying region of the intertidal flat. The model is demonstrated to be able to reproduce the classic theory of tidal-flat hydrodynamics of Friedrichs and Aubrey (1996) and to predict the turbidity at the tidal edge that is similar, qualitatively, to prior field observations. The Regional Ocean Modeling System (ROMS) is also utilized to simulate the same idealized tidal flat to evaluate its applicability in this environment. We demonstrate that when a small critical depth (h_{crit} =2 cm) in the wetting and drying scheme is adopted, ROMS is able to predict the main features of hydrodynamics and sediment-transport processes similar to that predicted by the RANS-VOF model. When driving the models with a symmetric tidal forcing, both models predict landward transport on the lower and upper flat and seaward transport in the subtidal region. When the very shallow region of the tidal edge is well resolved, both models predict an asymmetry of tidal velocity magnitude between the flood and the ebb that may encourage landward sediment transport on the flat. Further model simulation suggests that the predicted landward transport of sediment on the flat is mainly due to the settling-lag effect while the asymmetry of tidal velocity magnitude may add a lesser but non-negligible amount. When the bed erosion is limited by the availability of soft mud, the predicted transport direction becomes landward in both the subtidal region and on the flat. These results suggest that the tidal flow generally encourages landward transport while significant seaward transport may be caused by other mechanisms. Comparisons

with field observations show similarities in the net landward transport on the flat and enhanced stresses and suspended-sediment concentrations near the very shallow region of the tidal edge. The field results also indicate significant transport of sediment occurs through the channels, as a function of three-dimensional processes, which are not incorporated in the present idealized modeling.

1. INTRODUCTION

Intertidal flats create the critical linkage between the deeper part of the estuary (e.g., tidal channels) and the vegetated upper flat, e.g., salt marshes. The morphology of many tidal flats is in very subtle dynamic equilibrium (de Swart and Zimmerman, 2009; see Le Hir et al., 2000, for a review) and hence they are also very vulnerable to natural and anthropogenic influences. To preserve or even to reclaim intertidal habitat, it is critical to understand various mechanisms causing landward and seaward transport. This requires development of numerical modeling tools for predicting and managing the shallow estuarine ecosystem.

The classic equilibrium theory of intertidal flat morphology developed by Friedrichs and Aubrey (1996) (subsequently referred to as FA96) is based on pure kinematic analysis (mass conservation). According to FA96, the maximum tidal velocity magnitude U in the subtidal and the lower flat regions is calculated by

$$U = \frac{L\pi}{T}, \qquad x \le L/2 \tag{1a}$$

where L is the horizontal distance from the low to high water line and T is the tidal period (see also Fig. 1). At the upper flat, maximum tidal velocity magnitude is calculated by

$$U = \frac{2\pi}{T} L \left(\frac{x}{L} - \frac{x^2}{L^2} \right)^{1/2}, \qquad x > L/2 \qquad (1b)$$

FA96 provides simple and very useful descriptions that can be used to estimate the maximum tidal-flow velocity (or bottom stress) on a tidal flat and to explain the morphology of many existing intertidal flat systems.

To develop more process-based descriptions on the morphodynamics of these environments, various forcing mechanisms controlling tidally averaged landward and seaward sediment transport of intertidal mudflats have been investigated (e.g., Le Hir et al., 2000). The general understanding indicates that during calm conditions, tidal forcing alone (especially during spring tide) can cause landward transport and accretion of the upper flat (e.g., Christie et al., 1999; Bassoullet et al., 2000). During storm conditions, wind waves can enhance resuspension and may cause significant seaward sediment transport and erosion. More specifically, it is well known that tidal asymmetry, namely the flood (ebb) dominant tidal current can encourage landward (seaward) transport (e.g., Christie et al., 1999). In addition, tidal-averaged residual sediment transport can be further correlated with tidal velocity skewness and the phase difference between tidal velocity and tidal level fluctuations (i.e., Stokes drift; Uncles and Jordan, 1980; Son and Hsu, 2011b). Because of the shape of the tidal forcing, tidal asymmetry and velocity skewness are site dependent quantities and they can cause either landward or seaward transport. A more persistent landward transport mechanism on tidal flats is attributed to a non-local processes, called the settling-lag effect (e.g., van Straaten and Keunen, 1958; Postma, 1961), which gives a tidally-averaged residual transport directed toward an area of lower energy because it takes time for the suspended sediment to completely settle out. Consequently, the settling-lag effect gives net transport in the direction of lower maximum

bottom stress (or tidal velocity), and, when utilizing the classic theory of Friedrichs and Aubrey (1996), can explain accretion in the upper flat (Chen et al., 2010).

In reality, all the aforementioned mechanisms co-exist and it is not straightforward to determine the net transport. For example, at a mudflat of the Dollard estuary (Netherland) with ebb-dominant tidal currents, Dyer et al. (2000) measured net sediment transport to be flood-dominant, which could be due to the predominant settling-lag effect. The study of Ridderinkhof et al. (2000) in the ebb-dominant Ems-Dollard estuary (Netherland) suggests the net transport is also determined by sediment availability. For careful accounting of the settling-lag effect, several processes must be understood in detail, including the resuspension, advection and deposition of sediment on a tidal flat. The resuspension and advection processes may be directly related to commonly observed processes active at very shallow water depths near the land-water interface during both flood and ebb, which we defined in this study as turbid tidal edge (Christie and Dyer, 1998; Christie et al., 1999; Bassoullet et al., 2000; Mariotti and Fagherazzi, 2010; Nowacki and Ogston, this issue) or simply tidal edge. It is a signature of instantaneously large transport but its spatial variation and net transport must be closely related to the settling-lag effect.

Hence, there is a need to develop numerical models for tidal-flat hydrodynamics and sediment transport that can resolve all (or most) of these mechanisms in order to account for the competing effects. For tidal flats, numerical models are required to resolve very shallow water as very high suspended-sediment concentration is observed at times when data are compromised or non-existent due to sensor exposure (Mariotti and Fagherazzi, 2010; Nowacki and Ogston, this volume) and cannot capture the few minutes after (before) the passage of flood (ebb) tidal edge. Numerical models based on nonlinear shallow-water equations (NSWE) have been shown to be

capable of simulating the cross-shore hydrodynamics, sediment transport and morphodynamic processes in idealized tidal flats (Roberts et al., 2000; Pritchard et al., 2002; Pritchard and Hogg, 2003). Specifically, Pritchard and Hogg (2003) demonstrate that the NSWE model captures the turbid tidal edge, and the resulting sediment flux and morphodynamics can be explained by the settling-lag effects. However, NSWE models, even when extended to two dimensions (i.e., two-dimension flow in a horizontal plane, 2DH), remain based on a depth-integrated formulation. It may be suitable for a well-mixed tidal flat, but cannot be used to model a wider area of an estuary when salinity and temperature stratification become critical mechanisms driving the overall estuary circulations and sediment dynamics (e.g., Ralston and Stacey, 2007).

In the past decade, three-dimensional numerical modeling systems have become very useful tools to study coastal and estuarine hydrodynamics and sediment transport (e.g. Li et al., 2004; Warner et al., 2005; Harris et al., 2005; Ralston et al., 2010; Ralston et al., this issue). These numerical models (e.g., the Regional Ocean Modeling System (ROMS), Haidvogel et al., 2000) are mostly based on solving hydrostatic Reynolds-averaged Navier-Stokes (RANS) equations with a stretched, bottom-following coordinate system. They are very powerful tools to study estuarine circulation and sediment dynamics and the exchange between the estuary and continental shelf. However, their applicability in simulating very shallow water is uncertain. Although there have been technical advancement in the wetting and drying treatments in these modeling systems (e.g., Warner et al. 2008a), there are very few coastal and nearshore applications in shallow water (e.g., Chen et al., 2010). As a result, the effects of these wetting and drying treatments on shallow flow and sediment dynamics remain unclear.

In this study, two numerical models, originally designed to study processes at different scales, are utilized to study fine-sediment transport across intertidal flats. Firstly, we utilize a new numerical modeling approach for tidal-flat processes based on the Volume of Fluid (VOF) method (Hirt and Nichols, 1981) to track the free-surface evolution. A two-dimensional-vertical (2DV) numerical model with VOF capability (COBRAS, Cornell Breaking Wave and Structure; Lin & Liu, 1998), originally designed to resolve small-scale water-column processes, is revised in this study of tidal flow. The numerical model solves 2DV RANS equations with a k-ε turbulence closure and hence it will be called the RANS-VOF model in this paper. To understand the capability of a large-scale coastal modeling system in simulating large amounts of landward and seaward transport across the intertidal flats, ROMS is also utilized. Inter-comparisons of model results between RANS-VOF and ROMS for fine sediment transport across idealized intertidal flats are reported.

The RANS-VOF model is used to simulate processes of hydrodynamics and sediment transport across an idealized tidal flat with flow conditions similar to Willapa Bay (Nittrouer et al., this issue). High-resolution numerical model results are then used to investigate processes that occur at the turbid tidal edge. In particular, we study landward and seaward sediment fluxes and the relationship between the upper intertidal region and the lower completely submerged region. Because the VOF model is computationally expensive and can only be used in idealized conditions, the second objective is to carry out inter-comparisons between the results of RANS-VOF and ROMS. We evaluate the capability of ROMS in simulating hydrodynamics and sediment transport in tidal flats by changing the critical depth of the wetting and drying scheme. Finally, field data of flow velocity and suspended-sediment-concentration profiles measured in a

channel-flat system are presented in order to appreciate the complexity in the field condition and to test several qualitative features obtained in the idealized numerical study.

2. NUMERICAL MODELS

2.1 RANS-VOF MODEL

A 2DV-RANS model for sediment-laden flow with a k-ε turbulence closure is utilized here to study cross-shore fine sediment transport in intertidal flats. This numerical model is an extension of the wave model, COBRAS (Lin and Liu, 1998a) utilized to study various surf-zone wave problems (e.g., Lin and Liu, 1998b; Lara et al., 2006). The backbone of the COBRAS model is a two-dimensional Navier-Stokes solver with a volume of fluid (VOF) scheme for free surface tracking called RIPPLE, developed originally by Los Alamos National Laboratory (Kothe et al., 1991). This numerical model has recently been extended with a fine sediment-transport capability in order to study wave-mud interactions (Torres-Freyermuth and Hsu, 2010). In the present study, we revised the code used in Torres-Freyermuth and Hsu (2010) for tidal flow applications. In the dilute limit, which is the case here, the sediment transport formulation adopted in RANS-VOF is similar to that of ROMS where sediment concentration is calculated by mass conservation and sediment-induced density can drive gravity flow and cause damping of carrier flow turbulence.

2.1 .1 Model Formulation

The present model adopts the assumption of fine-grained sediment and hence the complete two-phase flow formulation for particle-laden flow can be significantly simplified (Balachandar and Eaton 2010; Torres-Freyermuth and Hsu 2010). The rigorous justification of this fine sediment approximation requires the particle response time (see equation (3)) to be smaller than the

Kolmogorov timescale. Particle response time is a measure of the timescale required for a single particle to follow the ambient fluid flow (Balachandar and Eaton, 2010). A simple example is demonstrated here to support our assumption. We consider fine-grained sediment transport in an intertidal mudflat where the settling velocity is no more than O(1) mm/s. The settling velocity can be calculated by Stokes law

$$W_s = \frac{(\rho^s - \rho)gd^2}{18\mu} \qquad (2)$$

where ρ is the fluid density, μ is the fluid viscosity, and g is the gravitational acceleration. If we consider silt transported as primary particles with grain size d=34 μm and sediment density ρ^s=2650 kg/m^3, the settling velocity is calculated to be 1 mm/s and the corresponding particle response time

$$T_p = \frac{W_s}{(1 - \rho/\rho^s)g} \qquad (3)$$

is only 1.6×10^{-4} sec. Considering a typical turbulent dissipation rate in a meso-tidal environment of ε=O(10^{-4}~10^{-3}) (Fettweis et al., 2006), the Kolmogorov timescale is only 0.03~0.1 sec, which is about two orders of magnitude larger than the particle response time. Similarly, if we consider a flocculated particle of size d=60 μm and floc density ρ^s=1250 kg/m^3 (using a fractal dimension 2.3 and primary particle size of 4 μm; Krenenburg, 1994), the resulting settling velocity is 0.5 mm/s and the particle response time is only $T_p=2.6\times10^{-4}$ sec. In summary, for a typical intertidal flat, fine sediments are almost passive to the carrier flow other than the effects of settling velocity. Hence, sediment transport can be calculated by mass conservation and the only effect of sediment on the carrier flow that needs to be considered is the sediment-induced density stratification (Ozdemir et al., 2010).

The numerical model is based on Reynolds-averaged two-dimensional-vertical formulation for fluid flow and suspended-sediment transport. The continuity equation is written as

$$\frac{\partial(1-\phi)}{\partial t}+\frac{\partial(1-\phi)u}{\partial x}+\frac{\partial(1-\phi)w}{\partial z}=0 \tag{4}$$

where ϕ is the sediment volumetric concentration, u is the flow velocity in the x- (streamwise or cross-shore) direction and w is the velocity in the z- (vertical) direction. The flow momentum equations in the streamwise and vertical directions are written as

$$\frac{\partial u}{\partial t}+u\frac{\partial u}{\partial x}+w\frac{\partial u}{\partial z}=-\frac{1}{\rho}\frac{\partial p}{\partial x}+\frac{1}{\rho(1-\phi)}\left(\frac{\partial \tau_{xz}^{f}}{\partial z}+\frac{\partial \tau_{xx}^{f}}{\partial x}\right) \tag{5}$$

and

$$\frac{\partial w}{\partial t}+u\frac{\partial w}{\partial x}+w\frac{\partial w}{\partial z}=-\frac{1}{\rho}\frac{\partial p}{\partial z}+\frac{1}{\rho(1-\phi)}\left(\frac{\partial \tau_{zz}^{f}}{\partial z}+\frac{\partial \tau_{zx}^{f}}{\partial x}\right)-\left[1+\frac{(s-1)\phi}{(1-\phi)}\right]g \tag{6}$$

where p is the fluid pressure, $s=\rho^{s}/\rho$ is the specific gravity and τ^{f} represents the fluid stresses, including viscous and turbulent stresses. The last term on the right-hand-side of equation (6) represents the sediment-induced buoyancy effect. Sediment concentration is calculated by mass balance:

$$\frac{\partial \phi}{\partial t}+\frac{\partial \phi u}{\partial x}+\frac{\partial \phi w}{\partial z}=\frac{\partial \phi W_s}{\partial z}+\frac{\partial}{\partial z}\left[\left(\frac{\nu_t}{\sigma_c}+D_c\right)\frac{\partial \phi}{\partial z}\right]+\frac{\partial}{\partial x}\left[\left(\frac{\nu_t}{\sigma_c}+D_c\right)\frac{\partial \phi}{\partial x}\right] \tag{7}$$

where ν_t is the eddy viscosity, σ_c is the Schmidt number and D_c is the viscous (Brownian) diffusion coefficient. Settling velocity W_s is calculated by equation (2). Hindered settling effects

are not important in this study because the maximum sediment concentration calculated is no more than 15 g/L (volumetric concentration 0.6%).

Closure of turbulent Reynolds stress is based on the eddy viscosity hypothesis:

$$\tau_{ij}^{f} = \rho(\nu + \nu_t)\left(\frac{\partial u_i}{\partial x_j} + \frac{\partial u_j}{\partial x_i}\right) - \frac{2}{3}\rho(1-\phi)k\delta_{ij} - \frac{2}{3}\rho\nu_t\frac{\partial u_l}{\partial x_l}\delta_{ij} \tag{8}$$

where i, j= 1, 2 for 2DV flow and δ_{ij} is the Kronecker delta. The eddy viscosity is further calculated by the k-ε closure

$$\nu_t = C_\mu \frac{k^2(1-\phi)}{\varepsilon} \tag{9}$$

where k is the turbulent kinetic energy (TKE), ε is the turbulent dissipation rate and C_μ is an empirical coefficient. The balance equations for k and ε are written as

$$(1-\phi)\left(\frac{\partial k}{\partial t} + \frac{\partial k u_j}{\partial x_j}\right) = \frac{\tau_{ij}^{f}}{\rho}\frac{\partial u_i}{\partial x_j} + \frac{\partial}{\partial x_j}\left[\left(\nu + \frac{\nu_t}{\sigma_k}\right)\frac{\partial(1-\phi)k}{\partial x_j}\right] - (1-\phi)\varepsilon + g\frac{\nu_t}{\sigma_c}(s-1)\frac{\partial\phi}{\partial z} \tag{10}$$

and

$$(1-\phi)\left(\frac{\partial \varepsilon}{\partial t} + \frac{\partial \varepsilon u_j}{\partial x_j}\right) = C_{\varepsilon 1}\frac{\varepsilon}{k}\frac{\tau_{ij}^{f}}{\rho}\frac{\partial u_i}{\partial x_j} + \frac{\partial}{\partial x_j}\left[\left(\nu + \frac{\nu_t}{\sigma_\varepsilon}\right)\frac{\partial(1-\phi)\varepsilon}{\partial x_j}\right] - (1-\phi)C_{\varepsilon 2}\frac{\varepsilon^2}{k} + C_{\varepsilon 3}^{*}\frac{\varepsilon}{k}g\frac{\nu_t}{\sigma_c}(s-1)\frac{\partial\phi}{\partial z} \tag{11}$$

These two equations are essentially the standard k-ε equations for particle-laden flow with small particle response time. The standard k-ε equations are developed with the main assumptions following Kolmogorov hypothesis for fully turbulent flow. The last terms of these two equations

represent the effect of sediment-induced density stratification on carrier turbulent flow, which is also a well-known mechanism for salt- or heat-stratified flow. If the Boussinesq approximation for dilute sediment flow (which is the case in this study) and the hydrostatic pressure approximation are adopted, the present governing equations and closures become similar to that typically used for coastal and estuary modeling, such as ROMS.

A continuous erosion/deposition approach is utilized as the bottom boundary condition for sediment concentration. Sediment erosion flux from the bottom is specified with the following formula

$$E = \beta\left(\frac{\tau_b(t)}{\tau_c} - 1\right) \qquad (12)$$

where β (m/s) is an empirical erosion flux coefficient and $\tau_b(t)$ is the bottom stress. In this study, a constant critical shear stress for erosion is adopted in most cases for simplicity. The logarithmic law for a rough bed is applied between the bed and the first half grid point above the bed to estimate bottom stress. The resulting bottom stress is further used as bottom boundary condition for the streamwise flow velocity (u) and to estimate the boundary condition for turbulent kinetic energy (k), turbulent dissipation rate (ε), and sediment erosion flux. More details on the bottom boundary conditions for boundary layer and sediment transport can be found in Torres-Freyermuth and Hsu (2010).

2.1.2 Numerical implementation

The 2DV-RANS-VOF model is based on a finite difference scheme, which is second-order accurate in spatial discretization. The mass and momentum equations are solved by the two-step

project method, a solution technique commonly used for incompressible Navier-Stokes equations. The fully explicit two-step project scheme is utilized in this study to save computational time and hence the temporal discretization is only first-order accurate. A central difference scheme is used for various diffusion terms in the governing equations and a combined upwind and central difference scheme is used for advection/convection terms. The time-step size is determined every computational cycle based on the Courant–Friedrichs–Lewy condition and the maximum time step is set to be no more than 0.05 sec.

The present model adopts a VOF variable, F(x,z,t), to describe the free surface (Hirt & Nichols 1981). For a grid cell completely occupied by water, F is defined to be 1.0. On the other hand, for a grid cell completely occupied by air, F=0. For an interface cell that is partly occupied by water and partly occupied by air, F represents the fraction of the volume occupied by water, i.e., 0<F<1. At every time step, the F value is updated by an advection equation of F(x,z,t):

$$\frac{\partial F}{\partial t} + u\frac{\partial F}{\partial x} + w\frac{\partial F}{\partial z} = 0 \tag{13}$$

The time-dependent free-surface location can be reconstructed from F. For any free-surface flow, equation (13) essentially represents the kinematic boundary condition of the flow. The VOF scheme is originally developed to resolve effectively the detailed interface dynamics of two phase flow (e.g., air and water). Because the F value within a grid point follows the mass balance via equation (13), the VOF scheme can describe free-surface flow within one grid point (in a grid-averaged sense). In this study, numerical experiments further suggest when the volume of fluid value in a grid cell is below about 0.3 and the cell is directly above the solid bottom, the advection of fluid to the adjacent cell can cause noise in velocity due to numerical

approximation. This numerical fluctuation may be minimized with a smaller time step or grid size. A cut-off value for the minimum F to be calculated in the numerical scheme is set to be F_{min}=0.01. A larger cut-off value of the VOF function can also be used to minimize the noise. More details of using volume of fluid approach for free-surface flow can be found in Hirt & Nichols (1981). The accuracy of the present numerical model, and particularly the VOF scheme in simulating shallow water process has been demonstrated in many prior studies, such as those describing swash zone processes (Lara et al., 2006), dam break waves (Shigematsu et al., 2004) and bore propagation over a slope (Zhang and Liu, 2008). The readers are referred to these earlier studies for more detailed model validations.

The numerical model utilizes a partial-cell treatment (Kothe et al., 1991) for solid obstacles in the computational domain. Although the partial-cell treatment provides a robust scheme to approximate solid boundaries of arbitrary shape, the numerical accuracy near the solid boundary is low, which is not appropriate for the present application where tidal bottom-boundary-layer processes need to be well-resolved. Hence, the computational domain is rotated with an angle equal to the slope of the flat so that the bed surface can be accurately resolved with a rectangle mesh system. The no-flux boundary condition and zero-gradient boundary condition are applied for the flow velocity, k, ε and sediment concentration at the free-surface. A zero value of fluid pressure is applied at free-surface. For the rest of the boundaries, the gradient of pressure is specified to be zero.

To improve the accuracy of the lower order scheme used in the RANS-VOF model, we use fine spatial resolution and a small time step. We carried out a grid refinement test and found that the resolution adopted here is appropriate to evaluate the tidally averaged sediment-transport rate. For the present vertical grid size (Δz =0.05 m, see Section 3.1), the numerical diffusion (or

numerical viscosity =10^{-5}~10^{-4} m^2/s) is at least one order of magnitude smaller than the eddy viscosity (O(10^{-3}) m^2/s). Hence, the present low-order numerical scheme is appropriate for RANS modeling where mixing is dominated by eddy viscosity/diffusivity.

2.2 REGIONAL OCEAN MODELING SYSTEM (ROMS)

As we will demonstrate next, the RANS-VOF simulations are computationally expensive. Due to this limitation, the RANS-VOF cannot be easily applied to realistic coastal problems with spatial scales over tens of kilometers. Hence, one of the main objectives of this study is to conduct inter-comparisons between RANS-VOF and ROMS models, and to evaluate the capability of ROMS, specifically the wetting and drying scheme, in simulating processes across the shallow-water region of the tidal flats.

ROMS is a three-dimensional, hydrostatic, primitive-equation ocean model that solves the Reynolds-averaged form of the Navier-Stokes equations on a horizontal orthogonal curvilinear Arakawa ‘‘C’’ grid and uses stretched bottom-following coordinates in the vertical direction. The model formulation, numerical schemes, and the implementations of turbulence closures and boundary conditions are described in Haidvogel et al. (2000), Shchepetkin and McWilliams (2005), Warner et al. (2005), and Marchesiello et al. (2001). ROMS incorporates a suspended-sediment transport module that has been validated against laboratory experiments (e.g., Warner et al., 2008a). Suspended sediment is incorporated in the fluid density calculation and hence sediment-induced density stratification can damp the flow turbulence in the two-equation turbulence closure. ROMS with the sediment module has been applied to a wide range of idealized and realistic coastal flow problems (e.g., Chen et al., 2009; Chen et al., 2010; Warner et al., 2008b) and has been demonstrated to have high skill in the simulation of observed

salinity, velocity and turbulence (Warner et al., 2005; Li et al., 2005; Hetland and MacDonald, 2008). Moreover, the numerical model is parallelized. Thus, computationally intensive modeling work can be completed efficiently.

For tidal-flat applications, we need to utilize the existing wetting and drying scheme in ROMS to model the region of very shallow flow depth (Warner et al., 2008a). In this numerical treatment, a critical depth h_{crit} is specified. When the water depth of a computation cell is smaller than h_{crit}, the cell is considered "dry" and the fluxes to the adjacent cells are blocked (Casulli and Cheng, 1992). Most prior studies specify a rather large h_{crit} to save computational time and to ensure the shallow water region of the domain does not affect the inner flow field of interest. In this study, ROMS is utilized to carry out an idealized cross-shore study on an intertidal flat and variable h_{crit} are specified.

There are several main differences between the RANS-VOF model and ROMS. Firstly, in the RANS-VOF model, the full RANS equations are solved without hydrostatic approximations. The present geometry has a very mild slope and hence the non-hydrostatic pressure effect may be of minor significance. The importance of the non-hydrostatic effect will be investigated later. Secondly, the Boussinesq approximation is adopted for sediment-induced buoyancy effects in ROMS. For the present study, sediment concentration is dilute and hence the effect of the Boussinesq approximation is negligible. Therefore, it is expected that the major difference between ROMS and RANS-VOF is due to the numerical treatment of the wetting and drying scheme in very shallow water. As discussed in Section 2.1.2, the VOF scheme is able to calculate shallow flow depth of about O(1) cm (in a grid-averaged sense) when a Δz=5cm is used. On the other hand, the minimum depth that can be resolved by ROMS is directly determined by h_{crit}. Our model comparison demonstrates that when a very small h_{crit}=2cm is

used, ROMS model results are similar to those simulated by RANS-VOF. In addition, the computational time required by ROMS at this small h_{crit} value is significantly smaller than that of RANS-VOF.

3 CROSS-SHORE TRANSPORT ON AN IDEALIZED INTERTIDAL FLAT

3.1 Geometry

In this study, we investigate cross-shore transport of fine sediment on intertidal flats using the RANS-VOF numerical model and ROMS. A schematic plot of the numerical model domain setup is illustrated in Figure 1. The idealized tidal flat has a constant slope of α and the initial (low tide) water level is set to be 3.5 m for all the runs. The initial water line intercepts with the flat at x=0 m at low water and the flow is driven by a prescribed sinusoidal tidal-level variation of tidal amplitude η (m) and tidal period of T=12 hours. Hence, the region of x<0 m is completely submerged during the tidal passage and is defined as the subtidal region. The horizontal distance from the low to high water line is $L=\eta/\alpha$. The lower flat is defined here as the region between x=0 and x=L/2 and the upper flat is defined as the region between x=L/2 and x=L. The hydrodynamics and sediment-transport processes that occur in these three regions, namely the subtidal region, the lower-flat region and the upper-flat region, are quite distinct and hence differentiating between them is a main focus of our numerical investigation.

Numerical runs focus on an idealized Willapa Bay where the tidal-flat slope is set to be α=0.0013 and the tidal range is set to be η=4.25 m. For RANS-VOF simulations, the grid size in the streamwise direction (x) and vertical direction (z) is set to be Δx=10 m and Δz=0.05 m, respectively. Grid refinement tests indicate that simulations with half the grid size only change the resulting sediment concentration by 10%. Hence, the main flow features have low sensitivity

to further grid refinement. For this set of grid resolution, the time step is typically around 0.01 sec. In the main numerical run (Case 1 in Table 1), the settling velocity is set to be a constant of W_s=0.5 mm/s and the critical shear stress is also set to a constant of τ_c=0.15 Pa (Hill et al., this issue; Wiberg et al., this issue). The bottom roughness in the numerical simulation is set to be K_s=2.4 cm (z_0=0.8 mm), which is commonly used in other numerical studies of tidal flat to consider small scale bedforms and runnels (e.g., Le Hir et al., 2000). Additional runs with different settling velocity and bed erodibility are also carried out in order to investigate the effect of these parameters in the resulting cross-shore sediment transport. A summary of all the model runs is given in Table 1.

Case 1 is further simulated by ROMS using different h_{crit} values in the wetting and drying scheme (h_{crit}=10, 5, 2 cm). Model results suggest ROMS can capture the main characteristics predicted by RANS-VOF (see Section 3.3), when a small h_{crit}=2cm is used (10 sigma layers in the vertical direction). At h_{crit}=2cm, the barotropic time step is 0.05 sec, which is larger than that used in RANS-VOF. Moreover, RANS-VOF requires a much smaller streamwise grid size of Δx=10 m due to the VOF scheme (as compared to Δx=100 m in ROMS). For a 3-day model time using 16 processors, ROMS requires 5 hours to complete the simulation, which is about 10~15 times faster than that of RANS-VOF. It is noted here that the most time-consuming computational task in RANS-VOF is to solve the non-hydrostatic pressure field. By examining the calculated pressure field by RANS-VOF, the hydrostatic pressure distribution in the present problem is a good approximation except very near the tidal edge. Due to the high computational cost, the RANS-VOF model is run for only three tidal cycles and the results shown here are for the third tidal cycle unless otherwise noted. Our analysis suggests results obtained for the third

tidal cycle are similar to those of the second cycle. For all the cases shown in this study, the tidal-averaged sediment-transport rate of the third cycle is within 5% difference from that of the second tidal cycle. More noticeable differences can be observed for cases of smaller settling velocity.

3.2 Model Results

3.2.1 RANS-VOF results

The hydrodynamics and suspended-sediment concentration results for Case 1 are presented as snapshots during flood and ebb (see Fig. 2 and Fig. 3). The numerical model predicts the turbid tidal edge during flood and ebb similar to prior studies (Christie and Dyer, 1998; Christie et al., 1999). The cross-shore distributions of the near-bed velocity (Fig. 2b and 3b) suggest the velocity magnitudes are more or less uniform in the lower flat but increase significantly approaching the tidal water's edge. The increased velocity magnitude is also correlated with an increase in sediment concentration. Small fluctuations in velocity near the tidal edge are numerical noise discussed in Section 2.1.1. During flood, the near-bed velocity increases by about 95% approaching the tidal edge (see Fig. 2b). Near-bed velocity is directly related to bottom stress and hence the increased near-bed velocity induces a significant amount of sediment resuspension. In this case, the sediment concentration at flood tidal edge is as large as 15 g/L. During ebb (Fig. 3b), the near-bed velocity increases (in magnitude) by about 75% as the tidal edge is approached, which is a lesser increase than that during flood. The maximum sediment concentration in the ebb tidal edge is about 11 g/L, generally consistent with observations at slightly greater water depths of >3 g/L during winter ebb tides in Willapa Bay (Boldt et al., this volume). The observed asymmetry between flood and ebb in the near-bed tidal velocity and

suspended-sediment concentration, subject to a completely symmetric tidal forcing, may cause non-zero tidally averaged sediment transport (see Section 3.3.3).

Model results are compared with the analytical theory of FA96 (see equations (1a) and (1b)) for the cross-shore distribution of maximum tidal velocity over the entire tidal cycle. For Case 1, $L=\eta/\alpha=3270$ m and hence U=23.8 cm/s. Model results of depth-averaged cross-shore distribution of streamwise velocities over the entire tidal cycle (every 20 minutes interval) are plotted in Figure 4 (black curves) along with theoretical maximum values, i.e., equations (1a) and (1b) suggested by FA96. The numerical model predicts the maximum cross-shore velocity distribution (see the envelope of the black curves) that is consistent with FA96 for both flood and ebb conditions. The landward reduction in the maximum cross-shore velocity is anticipated to drive net landward sediment transport through the settling-lag effect (e.g., van Straaten and Keunen, 1958; Postma, 1961).

For $x \leq L/2$, numerical model results agree very well with FA96. For $x > L/2$, we observe some discrepancies. Specifically, the numerical model predicts a greater maximum depth-averaged velocity greater than that predicted by FA96 around the most landward extent of the tidal flow ($x>2900$ m). However, this occurs toward the end of flood where the overall magnitude of velocity is already smaller than that during mid flood, and this region is also of very shallow flow depth (no more than 10 cm or two grid points). It slightly increases landward transport closer to the upper flat but does not affect the net sediment transport (see Section 3.3.3). On the other hand, during ebb, the numerical model predicts smaller (in magnitude) velocities throughout the entire upper flat (also the upper part of the lower flat) compared to the theoretical value of FA96 ($1100\text{m}<x<3270\text{m}$). It can be qualitatively inferred that the reduction of velocity magnitude during ebb may cause less resuspension during ebb and therefore net

landward transport and accretion in the mid and upper flats. As we will investigate in more detail later, this asymmetric mechanism acts concurrently with the settling-lag effect to cause the observed landward transport.

In summary, in the very shallow water region (water depth $\approx<$ 30 cm), processes that occur at the flood and the ebb tidal edge are quite different. The numerical models predict the velocity at flood tidal edge in agreement with that predicted by FA96, or larger toward the end of the upper flat because of the existence of the sharp edge that is slightly concave downward due to friction (see Fig. 2a). The angle of contact at the tidal edge is larger than the flat slope and velocity must increase to conserve mass before the flow is dissipated by friction. On the other hand, the tidal velocity at ebb tidal edge is weaker than that predicted by FA96 (or than that during flood) because of the existence of a tail, i.e., slightly convex upward profile (see Fig. 3a). The tail region provides a transition of free-surface slope from horizontal (i.e., slope=0) to a slope close to that of the flat. Due to this mild transition and friction, the tidal velocity magnitude at the tidal edge becomes smaller than that predicted by FA96 as well as that during flood.

Time series at the landward end of the lower flat (x=1208 m, see top panel in Fig. 5) clearly shows high sediment concentration during the passage of flood and ebb tidal edge. However, asymmetries between flood and ebb can be observed. Based on the time series of bottom stress (middle panel in Fig. 5), as the tidal edge passes this location, the peak magnitude of bottom stress during flood is 50% larger than that during ebb. However, the duration of time when the bottom stress pulse exceeds the critical value for resuspension (τ_c=0.15 Pa, represented by the dashed line) is shorter during flood (1.2 hour) than that during ebb (1.9 hour). This is consistent with the previous observation that the flood tidal edge is sharper while the ebb tidal edge is more gradual. Interestingly, the duration of noticeable sediment concentration detected

by the numerical sensor ($c>10^{-3}$ g/L; see the color plot in the top panel of Fig. 5) is longer during flood (~2.8 hours) than during ebb (no more than 1.6 hours). During flood, not only is there a period of high suspended-sediment concentration at the first 1.2 hour of flooding (t=2.4~3.6 hr) associated with local resuspension (correlated with the period of $\tau_b>\tau_c$), but also there is a period following when noticeable sediment concentration (~O(0.1) g/L) is observed while $\tau_b<\tau_c$. The concentration decays slowly in time for another 1.6 hours. Therefore, there is a noticeable amount of sediment advected landward through this location during flood, which eventually settles. This description essentially represents the classic settling-lag mechanism. On the other hand, the timing of high concentration during ebb tidal edge passage is directly related to the period of $\tau_b>\tau_c$, suggesting most of the observed high sediment concentration may be due to local resuspension, and advection of sediment from the more landward region during ebb may be of less importance at this location. Vertical profiles of velocity, sediment concentration and turbulence intensity (see subpanels in the third row of Fig. 5) suggest that in comparison to the ebb condition, the suspended-sediment concentration during flood is larger while turbulence intensity becomes smaller due to damping of turbulence via sediment-induced density stratification. Moreover, velocity profiles near the passage of tidal edge for both flood and ebb do not follow the logarithmic law reconstructed via the same roughness and local friction velocity obtained in the numerical model. The velocity near the tidal edge on both flood and ebb is larger than that predicted by the logarithmic law. Hence, drag reduction due to sediment-induced stratification is observed here.

A time series obtained from the subtidal region (location x=-92 m; see top panel in Fig. 6) clearly shows different features when compared to that obtained from the lower flat. Notice that this is the location where the bed is always submerged throughout the tidal cycle. Bed

sediment is resuspended around t=1.5 hour after the beginning of the tidal flow, which is directly correlated with the time when bottom stress exceeds critical value (see middle panel). Hence, it can be concluded that sediment suspension in the subtidal region does not occur at the beginning of the tide (i.e., there is no tidal water's edge). During ebb, strong sediment suspension occurs at t=8.7 hour, more or less coincident with the instant when bottom stress exceeds the critical value, indicating the onset of local resuspension.

However, sediment concentration during ebb is about 2 times larger than that during flood (see top panel and concentration profile in the 3rd panel). Noticeable sediment concentration ($c>10^{-3}$ g/L) during ebb lasts until t=11.4 hr, although the bottom stress is less than the critical value at t=10.6 hr, suggesting that sediment is advected from more landward locations. The sediment advection is due to the ebb tidal pulse that occurred just upstream on the lower flat (at locations x>0). The asymmetry in the magnitude and duration of elevated sediment concentration is expected to drive net seaward transport in the subtidal region and will be discussed in more detail later. Based on the sediment concentration and velocity profiles (see the 3rd row in Fig. 6), it can be observed that suspended-sediment concentration is smaller and more well-mixed in the water column compared to the profiles at the landward end of the lower flat. The velocity profiles in the subtidal region are also closer to the logarithmic law.

3.2.2 ROMS results for Case 1

Using a critical depth of h_{crit}=10 cm (typically recommended value; J. Warner, personal communication; Chen et al., 2010), ROMS under-predicts the magnitude of the depth-averaged streamwise velocity maximum compared to the theory of FA96 (Fig. 7a). More importantly, the predicted maximum velocity magnitude is more or less symmetric between flood and ebb, which

is inconsistent with that predicted by RANS-VOF. As mentioned previously, this asymmetry may contribute net landward sediment transport, and cannot be captured by ROMS with a large critical depth.

When using a much smaller critical depth of h_{crit}=2 cm, ROMS predicts the magnitude of the depth-averaged velocity maximum similar to that calculated by the RANS-VOF model (Fig. 7b). Firstly, the maximum during flood matches well with FA96 theoretical value, and secondly, the asymmetry of maximum magnitudes between flood and ebb is also captured and compares fairly well with RANS-VOF model results. However, near the tidal edge during flood, undulations are observed due to non-hydrostatic effects that are not properly represented in ROMS. As we shall demonstrate next, it appears that such undulations are of minor importance to the predicted flow pattern and the resulting net sediment transport rate. Time series of the sediment-concentration profile and bottom stress at the landward end of the lower flat computed by ROMS with h_{crit}=2 cm are shown in Figure 8. This location is similar to that shown in Figure 5 for the RANS-VOF model results (i.e., x=1208 m). Here, ROMS is able to predict higher bottom stress and suspended-sediment concentration during the passage of the flood and ebb water's edge. More importantly, the predicted asymmetry of suspended-sediment concentration, namely the gradual decay of sediment concentration after the passage of flood tidal edge and the abrupt increase of sediment concentration during the passage of ebb tidal edge, is similar to that predicted by the RANS-VOF model. As can be seen in the bottom panel of Figure 8, the sharp transition of bottom stress near the wet-dry boundary is better represented with a small h_{crit} than with a larger one. It can be reasonably expected that more detailed small-scale features predicted by the RANS-VOF model can be reproduced by ROMS by further increasing the resolution and decreasing h_{crit}. Here, we demonstrate that when the wetting and drying region is of main

interest, such as in tidal-flat applications, a small h_{crit} can be used and ROMS can predict the main features of tidal flat hydrodynamics and sediment transport similar to that computed by the RANS-VOF model.

3.3 Discussion

3.3.1 Effect of sediment-induced density stratification

Using the RANS-VOF model results obtained at x=1208 m, Figure 9 further illustrates the effect of sediment-induced density stratification on the resulting flow velocity, suspended-sediment concentration and turbulence-intensity profiles (see Case 2 in Table 1). Near the passage of the flood tidal edge with a flow depth of no more than half a meter, sediment-induced density stratification has significant effects on the resulting flow field and sediment transport (see (a1)~(a3) of Fig. 9). Without considering sediment-induced density stratification terms in the k and ε equations, the predicted turbulence intensity is about 20% larger (TKE becomes about 50% larger) and the resulting suspended-sediment concentration is about 70% to a factor of two larger. In addition, when sediment-induced density stratification is not considered, the predicted velocity profile more closely follows the logarithmic law (compare red-dashed and red-doted curves in (a1) of Fig. 9) but is not completely identical to it. Hence, it is clear that the enhanced velocity predicted by the numerical model near the tidal edge (compare black-solid and black-dashed-dotted curves) is due to both sediment-induced density stratification (drag reduction) and acceleration (temporal and spatial) at the tidal edge. At a later time when the tidal edge has long passed the sensor and the flow depth become greater than 1.5 m (see (b1)~(b3) in Fig. 9), the predicted sediment-concentration profile is well-mixed in part due to the relatively low sediment concentration (significantly lower than 1 g/L). In this case, turbulence intensity is only slightly

reduced by sediment-induced density stratification and the predicted velocity profiles are close to the logarithmic law. In summary, suspended-sediment concentration at the turbid tidal edge can be much larger than O(1) g/L and hence it is critical to consider sediment-induced density stratification in modeling.

3.3.2 Exchange between flat and subtidal regions

Figure 10 further illustrates the exchange of sediment between the lower flat (x=1208 m) and the subtidal region (x=-692 m) based on RANS-VOF model results of Case 3 (see Table 1). Compared to Case 1, which has been the main focus of the discussions so far, Case 3 has a smaller settling velocity and hence more sediments are kept suspended in the water column throughout the entire tidal cycle (compare the upper panels of Fig. 10 and Fig. 5) and therefore is more subject to the settling-lag effect and exchange between the intertidal and the subtidal regions.

As described in Figure 5, bottom stress at the lower flat (x=1208 m) drops below the critical value for erosion at around t=3.6 hr. For Case 3 (Fig. 10), significant concentrations of sediment remain in the water column throughout the entire flood period, suggesting a more pronounced settling-lag effect for sediments of smaller settling velocity, consistent with the theory (e.g., de Swart and Zimmerman, 2009). In the subtidal region (see lower panel), a strong ebb sediment pulse occurs in the last three hours of the tidal cycle. In contrast, on the lower flat the ebb sediment-concentration peak occurs when tidal level is already low (η<2.5 m) and the upper flat is already emerged. This flat-channel picture is quite similar to prior field observations (e.g., Bassoullet et al., 2000) and recent field study at Willapa Bay (Mariotti and Fagherazzi, 2010; Nowacki and Ogston, this volume). It should also be noted here that during low slack as

tidal flow velocity reverses to flood, suspended-sediment concentration continues to be $O(10^{-3})$ g/L. The residual sediment concentration during low slack, which is actually larger for farther seaward locations (e.g., $O(10^{-2})$ g/L at location x=-692 m, not shown here), are due to the low settling velocity specified in this case. These residual sediments may contribute landward transport as the tidal velocity becomes landward during flood. However, in reality, channels and runnels may effectively deliver sediment that was suspended via the ebb tidal pulse out of the immediate channel network and hence the present numerical study is certainly too idealized to address the importance of this mechanism.

3.3.3 Tidally averaged cross-shore transport rate

An examination of the tidally averaged sediment transport rate for Case 1 (Fig. 11, square symbols) calculated by the RANS-VOF model suggests landward transport occurs for x>320 m (most of the lower flat and the entire upper flat), and seaward transport occurs for x<320 m (seaward end of the lower flat and the subtidal region). As discussed in the previous section, the observed landward transport in mid and upper flats can be due to two main mechanisms: the settling-lag effect and the asymmetry of depth-averaged cross-shore velocity magnitude between flood and ebb. Based on the envelopes of speeds (see Fig. 4 and Fig. 7b), flood velocities exceed those during ebb at locations between the landward end of the lower flat and the upper flat, resulting in net landward transport there. Because the ROMS model result for h_{crit}=10 cm does not resolve the very shallow water region and the asymmetry of depth-averaged cross-shore velocity magnitudes between flood and ebb (see Fig. 7a), inter-comparison of the ROMS model results computed with h_{crit}=10 cm and h_{crit}=2 cm allows us to qualitatively estimate the importance of resolving the very shallow region of the tidal edge on the tidally averaged

transport rate. Using h_{crit}=2 cm, the predicted landward transport rate is about 40~50% larger than that using h_{crit}=10 cm (See Fig. 12). However, this 40~50% increase in net transport rate is not only due to the tidal asymmetry in velocity. The asymmetry of bottom stress near the wet-dry interface is only about 10% (e.g. Fig. 8 lower panel, h_{crit}=2 cm case). Hence, a significant portion of the increase in transport may still be associated with the settling-lag effect. We would like to clarify that once sediments are suspended, landward transport is obtained through advection and the settling-lag effect, regardless of asymmetry in velocity (and bottom stress). In other words, it is difficult to separate the asymmetry effect and the settling-lag effect. Here, we demonstrate that resolving the very shallow water region may contribute additional landward transport of 40~50%. However, we believe part of the additional transport can be still associated with the settling-lag effect.

Seaward transport is observed at the seaward end of the lower flat and the subtidal region for Case 1 (see Fig. 11; x<320 m). This seaward transport can be expected due to the downslope advection of the ebb tidal-edge pulse discussed previously (see Figs. 5 and 10). Figure 11 further presents the tidally averaged sediment transport rate for Case 3 of lower settling velocity (crosses). Landward transport is predicted for x>500 m and seaward transport is obtained for x<500m, consistent with that of Case 1. However, the magnitude of net landward and seaward transport for Case 3 is about 4 times larger than that of Case 1 due to the smaller settling velocity. On the other hand, for Case 4 with a larger settling velocity (circles), similar landward and seaward transport patterns are predicted but the magnitude is about 3~5 times smaller than that of Case 1. The dependence of the tidally averaged transport rate on settling velocity is consistent with the increased intensity of ebb tidal-edge pulse when a smaller settling velocity is used. The increase in flood dominance (landward transport) as settling velocity decreases is also

consistent with typical geomorphic observation that tidally dominated flats often show coarser grain size in the seaward direction. In all three cases, we observe divergence of the tidally averaged sediment-transport rate near the subtidal and lower-flat region (x=0~500 m), implying erosion there and a convex-upward morphological profile, which is also consistent with typical tide-dominated flat profiles (Roberts et al., 2000; Pritchard and Hogg, 2003; Friedrichs, 2011).

Floc dynamics are not considered in the present modeling study. However, the dependence of net sediment transport rate on settling velocity may allow us to qualitatively estimate the effect of floc dynamics. The control of floc size, in general, depends on sediment concentration and flow turbulence. For relatively low energy conditions, such those on a tidal flat without significant wave stresses, floc size is approximately proportional to sediment concentration (e.g., Winterwerp et al., 2006; Son and Hsu, 2011a). Higher sediment concentration is predicted by the present models near the tidal edge, and therefore increased floc size would be most likely to occur in this zone. Predicted sediment concentration is also larger during flood than that of ebb, and enhanced floc settling during the flood and will tend to decrease this difference, and slightly reduce the net sediment transport. We can conjecture that when flocculation is considered, the predicted magnitude of both landward and seaward transport fluxes might become smaller. However, the general trend may be very similar to the results shown here for constant settling velocity.

Erodibility parameters of the mud bed, e.g., the parameterization of critical shear stress of erosion τ_b, is another poorly constrained quantity. Numerical experiments using the RANS-VOF model were further carried out to study the effect of bed erodibility on the resulting transport rate. Using Case 1 as the reference case, Case 5 simply tests the effect of lowering the critical

shear stress to τ_b=0.13 Pa. In general, reducing the critical shear stress by more than 30% (to <0.11 Pa) increases the magnitude of both the landward and seaward transport, and whether it has a preferred effect on the specific direction is not obvious (not shown). However, by only reducing the critical shear stress by about 15%, as in Case 5, it is clear that reduced critical shear stress encourages seaward transport (see Fig. 13, circles). For Case 1, there exists a period of no sediment resuspension between the slack tide and early ebb (see Fig. 5, t=6~8.2 hr). Reducing the critical shear stress reduces this period of no suspension during early ebb and hence encourages more seaward transport.

Due to consolidation, the critical shear stress increases as more sediment is eroded from the bed. Hence, critical shear stress is suggested to be parameterized as an increasing function of the total eroded mass, M (Sanford and Maa, 2001; Stevens et al., 2007; Wiberg et al., this issue). Typically in a tidal mudflat, the surface layer of the mud bed is of high erodibility because it is constantly being eroded and deposited every tidal cycle. Once this soft mud layer is removed, the critical shear stress increases sharply. Hence, we carry out another numerical experiment in Case 6 with τ_b=0.15 Pa, but only a limited amount of sediment of 0.03 kg/m^2 is allowed to be eroded (i.e., in equation (11) once M>0.03 kg/m^2, E is set to be zero; P. Wiberg, personal communication). Due to the limitation on erosion, the amount of available sediment to be eroded becomes significantly smaller every tidal cycle. Hence, the tidally averaged sediment transport rate, averaged over the first tidal cycle, is shown in Figure 13 (∇ symbol). Model results suggest that constraining the amount of erosion leads to a smaller tidally averaged sediment transport rate but more importantly, the resulting transport rates become landward-directed throughout almost the entire sub-tidal and intertidal regions of the tidal flat. On further examination, the model results in Case 1 (unlimited erosion) suggest that a considerable amount

of landward transport from the subtidal region to the lower flat occurs during flood tide and causes a noticeable amount of deposition. During late ebb, these new deposits in the lower flat are further resuspended and advected causing seaward transport in the subtidal region. However, due to the limited erosion constraint in Case 6, the amount of sediment resuspended and advected from the subtidal region to the lower flat is much smaller. This causes only a limited amount of sediment in the lower flat to be available for resuspension and advection to the subtidal region during ebb. Hence, seaward transport in the subtidal region is not observed when a limited erosion constraint is imposed. It is also noted here that for Case 6 of limited erosion, the tidally averaged transport rate for the second and third tidal cycle have a shape similar to that of Case 1 (i.e., seaward transport in the subtidal and lower portion of the lower-flat region and landward transport in the upper flat and upper portion of the lower flat) but with a significantly smaller magnitude (not shown).

In summary, when a limited erosion constraint is incorporated, tidal forcing in a tidal flat encourages landward transport predominately due to settling-lag effects. Significant seaward transport is not observed and hence we believe the dominant seaward transport mechanism in a tidal flat may be due to other factors such as variations in spring and neap tide, large-scale circulation features, and surface waves (Le Hir et al., 2000; Roberts et al., 2000; see also Nowacki and Ogston, this volume; Mariotti and Fagherazzi, this volume).

3.4.3 Field implications

The numerical model investigation presented in the previous sections provides mechanisms causing net landward and seaward sediment transport. Comparison of model results to field observations is challenging as the natural environment contains complexities due to the

three-dimensional nature of tidal flats, especially the existence of channels, which are not considered in the idealized numerical modeling. However, there remains a need to refer to data measured in the field, at least qualitatively, in order to evaluate the applicability of the findings obtained from idealized modeling in explaining realistic tidal-flat sediment-transport processes. Moreover, data described in Nowacki and Ogston (this volume) suggest the presence of the tidal-edge dynamic that is seen in both the RANS-VOF and ROMS models. And these detailed models allow an interpretation of processes that occur at shallow water depths where quality measurements are typically limited due to instrumentation capabilities.

As part of the field study, current and backscatter measurements at a channel/flat pair of sites were made with a 2 Mhz current profiler. Details of data collection are contained in Nowacki and Ogston (this volume), and the example in Figure 14 depicts a 12-hour tidal cycle in which wave heights were nominally zero from the July 2009 deployment. The upward-looking velocity profilers recorded 2-min averages of 25 Hz data every 10 min. Data contaminated by acoustic interaction with the water surface and out-of-water data were removed. We use the uncalibrated (but range corrected) acoustic backscatter to discuss relative concentrations of suspended sediment over the tidal cycle. Estimates of bed shear stress were obtained using the logarithmic law of the wall and the uncontaminated velocity at 30 cm above the seabed, with a bed roughness of 2.4 cm, consistent with the RANS-VOF model formulation. Although these estimates may not be accurate because of the bed roughness estimate and noise in the velocity data, they allow a discussion of the temporal patterns of bed stress observed on the tidal flats due to tidal currents. Putting the tidal range at the sites into the idealized numerical model set up would place the channel sensors at x~150 m and the flat sensors at x~1300 m within the model domain (Fig. 1). In other words, both sensors are located above the subtidal region and the main

differences between the observed data from these two sensor are due to more complex 3D channel-flat effect that are not incorporated in the idealized numerical model results.

On the flat, velocities are highest at the lowest tidal elevations monitored on both flood inundation and ebb dewatering, indicative of the tidal edge processes (Fig. 14, right panels). Velocities appear slightly stronger on the flood than ebb tide, leading to greater peak magnitude of stress on the flood tide. This feature is consistent with idealized model results (see Figs. 5 and 8). The backscatter suggests significantly greater concentrations of sediment put in suspension on the flood tide than on the ebb under these field conditions. On the other hand, the idealized model results suggest suspended-sediment concentration during flood is only about 20~30% larger, although the duration of sediment in suspension is also longer than that during ebb. Qualitatively, both field-measured data and idealized model results indicate net landward transport of sediment.

The channel data is more complex as it is dominated by three-dimensional effects of flow within the channel/flat complex and concentrations of sediment are associated with resuspension in the channel and on the nearby flat (Fig. 14, left panels). At this location, the tidal edge effect during flooding tide is not evident in the velocity data, but the enhanced suspended-sediment concentrations prior to the velocity pulse at mid tide suggests that the tidal edge likely caused resuspension at very shallow water depths when the velocity sensors could not produce reliable data. The suspended-sediment concentration associated with the tidal edge is predicted in the model to persist for a longer period of the flood tide than the ebb. In the observations, this signal is overwhelmed by the concentrations associated with the velocity pulse at mid tide. On the ebb tide, two peaks in bed stress are seen, one associated with the ebb-tide pulse (at ~9.8 hours after low tide) discussed in Nowacki and Ogston (this volume), and the other likely associated with

the tidal-edge pulse (at ~11 hours after low tide) that is predicted in the idealized model efforts here. This time series suggests significant seaward transport during ebb takes place mostly due to a mid-tide velocity pulse observed in the channel but not on the flat. The critical role of the three-dimensional effects of channels in delivering sediment seaward is not incorporated in the idealized numerical modeling.

Tidal flats, such as those in Willapa Bay, consist of a complex system of flat surfaces intersected by channels. As such there are multiple seabed gradients on the flat with differing spatial scales that are not captured in an idealized model. The three-dimensional interaction of flow between the channels and flat surfaces varies with tidal elevation (e.g., Nowacki and Ogston, this volume; Mariotti and Fagherazzi, 2010) and thus comparison of the idealized models presented here with field data shows intricacies not intended to be evaluated in the idealized study. The complexities of tidal flats intersected by channels are not incorporated in the present idealized model study. Hence, findings revealed in the idealized model study must be verified with field observation. Comparison with field data measured above the subtidal region on the flat and in the channel suggest model results of landward sediment transport during flood is more or less consistent with field observation. However, in this case, significant seaward delivery of sediment during ebb occurs mostly in the channel not on the flat. In summary, high-resolution model results allow us to evaluate the important processes associated with the tidal edge that is difficult for sensors to capture in the field, but cannot be used to generalize all of the tidal-flat transport processes. Effective incorporation of channels in a realistic numerical modeling of tidal flat is a critical challenge for future work.

4 CONCLUSION

We investigate sediment transport across idealized intertidal flats using two numerical models and field observations. A new numerical modeling approach for tidal-flat processes based on the Volume of Fluid (VOF) method is utilized to resolve processes at tidal water's edge with very shallow flow depth. The numerical model predicts the turbid tidal edge qualitatively consistent with field observations. Model results also reveal an asymmetry between flood and ebb maximum tidal velocity magnitude, which encourages landward transport.

Through inter-comparison with the RANS-VOF model, we demonstrate that ROMS is also capable of predicting the main hydrodynamics and sediment-transport features of the turbid tidal edge provided that a very small critical depth h_{crit} is used in the wetting and drying scheme. Numerical experiments using ROMS with different values of h_{crit} suggest that resolving the shallow water region of the turbid tidal water's edge (hence the asymmetry between flood and ebb maximum tidal velocity) contributes no more than 40~50% of the additional landward transport. This additional transport is certainly non-negligible but is smaller than the settling-lag effect. When a limited erosion constraint is incorporated, tidal forcing appears to cause net landward transport and hence we conclude that the main seaward transport mechanism in a tidal flat is due to effects not incorporated in the model (e.g., larger-scale three-dimensional circulation, surface wave effects, and variation in tidal cycles).

5 ACKNOWLEGEMENT

This study is supported by U.S. Office of Naval Research (Littoral Science and Optics program manager Dr. Thomas Drake) as part of the Tidal Flat DRI (N00014-09-1-0134; N00014-11-1-0270). SNC received partial support from Taiwan's National Science Council under grant NSC

100-2119-M-002 -028. We would also like to thank Dan Nowacki and Patricia Wiberg for useful discussions and four anonymous reviewers for their careful reviews and constructive comments.

6 RERERENCES

Balachandar, S., Eaton, J. K., 2010. Turbulent dispersed multiphase flow. *Annu. Rev. Fluid Mech.* 42, pp. 111-133.

Bassoullet, Ph., Le Hir, P., Gouleau, D., Robert, S., 2000. Sediment transport over an intertidal mudflat: field investigations and estimation of fluxes within the "Baie de Mareenes-Oleron" (France), Cont. Shelf Res., 20, 1635-1653.

Boldt, K., Nittrouer, C., Ogston, A., Seasonal transfer and net accumulation of fine sediment on a tidal flat approaching sea level: Willapa Bay, Washington, Cont. Shelf Res., in review for special issue.

Cantero, M. I., Balachandar, S., Cantelli, A., Pirmez, Parker, G., 2009. Turbidity current with a roof: direct numerical simulation of self-stratified turbulent channel flow driven by suspended sediment. J. Geophys. Res. 114, C03008.

Casulli, V. and Cheng, R., 1992. Semi-implicit finite difference methods for three-dimensional shallow water flow. *International Journal for Numerical Methods in Fluids* 15, 629–648.

Chen, S. N., Sanford, L. P., and Ralston, D. K., 2009. Lateral circulation and sediment transport driven by axial winds in an idealized, partially mixed estuary. *J. Geophys. Res.*, 114**,** doi:10.1029/2008JC005014.

Chen, S.-N., Geyer, W. R., Sherwood, C. R., Ralston, D. K., 2010. Sediment transport and deposition on a river-dominated tidal flat: an idealized model study, J. Geophys. Res., doi:10.1029/2010JC006248.

Christie, M. C., Dyer, K. R., 1998. Measurements of the turbid tidal edge over the Skeffling mudflats, in Black, K. S., Paterson, D. M., and Cramp, A. (eds) *Sedimentary Processes in the Intertidal Zone*, Geological Society, London, Special Publication, 139, 45-55.

Christie, M. C., Dyer, K. R., and Turner, P, 1999. Sediment flux and bed level measurements from a macro tidal mudflat. *Estuarine, Coastal and Shelf Sciences*, 49, 667-688.

Dyer. K. R., Christie, M. C., Feates, N., Fennessy, M. J., Pejrup, M., and van der Lee, W., 2000. An investigation into processes influencing the morphodynamics of an intertidal mudflat, the Dollard Estuary, the Netherlands: I. hydrodynamics and suspended sediment, Estuarine, Coastal and Shelf Science, 50, 607-625.

Fettweis, M., Francken, F., Pison, V., Van den Eynde, D., 2006. Suspended particulate matter dynamics and aggregate sizes in a high turbidity area. *Marine Geology*, *235*, 63-74.

Friedrichs C. T., Aubrey. D. G., 1996. Uniform bottom shear stress and equilibrium hyposometry of intertidal flats, in Mixing in estuaries and coastal seas, C. Pattiaratchi (eds), American Geophysical Union, p.405–429.

Haidvogel, D. B., Arango, H. G., Hedstrom, K., Beckmann, A., Malanotte-Rizzoli, P., Shchepetkin, A. F., 2000. Model evaluation experiments in the North Atlantic Basin: simulations in nonlinear terrain-following coordinates. Dynamics of the Atmosphere and Oceans 32, 239–281.

Harris, C. K., Traykovski, P. A., and Geyer, W. R., 2005. Flood dispersal and deposition by near-bed gravitational sediment flows and oceanographic transport: A numerical modeling study of the Eel River shelf, northern California, J. Geophys. Res., 110, C09025, doi:10.1029/2004JC002727.

Hetland, R. D., MacDonald, D. G., 2008. Spreading in the near-field Merrimack River plume. *Ocean Modeling*, 21**,** 12-21.

Hill P., Newgard, J., Law, B., Milligan, T., Linking suspended floc dynamics to the spatial distribution of sediment texture on the Shoalwater Bay tidal complex in Willapa Bay, Washington, Continental Shelf Res., in review for special issue.

Hirt, C. W., Nichols, B. D., 1981. Volume of fluid (VOF) method for the dynamics of free boundaries. J. Computational Phys., 39, 201-225.

Kothe, D. B., Mjolsness, R. C., and Torrey, M. D., 1991. RIPPLE: A computer program for incompressible flows with free surfaces, LA-12007-MS, Los Alamos Natl. Lab., Los Alamos, N.M..

Kranenburg, C., 1994. The fractal structure of cohesive sediment aggregates, *Estuarine Coastal Shelf Sci.*, *39*, 451-460.

Lara, J. L., Losada, I. J., Liu, P. L.-F. 2006. Breaking waves over a mild gravel slope: Experimental and numerical analysis, J. Geophys. Res., 111, C11019, doi:10.1029/2005JC003374.

Lee, S.-C., Mehta, A. J., 1997. Problems in characterizing dynamics of mud shore profiles. Journal of Hydraulic Engineering 123 (4), 1–11.

Le Hir, P., Roberts, W., Cazaillet, O., Christie, M., Bassoullet, P., Bacher, C., 2000. Characterization of intertidal flat hydrodynamics, Cont. Shelf Res., 20, 1433-1459.

Li, M., Zhong, L., Boicourt W. C., 2005. Simulations of Chesapeake Bay estuary: Sensitivity to turbulence mixing parameterizations and comparison with observations. J. Geophys. Res., 110, C12004, doi:10.1029/2004JC002585.

Lin, P., Liu, P. L.-F., 1998. A numerical study of breaking waves in the surf zone. *J. Fluid Mech*., Vol. 359, 239-264.

Marchesiello, P., McWilliams, J. C., Shchepetkin, A., 2001. Open boundary conditions for long-term integration of regional oceanic models. *Ocean Modeling*, 3, 1-20.

Mariotti, G., Fagherazzi, S., 2010. Asymmetric fluxes of water and sediments in a mesotidal mudflat channel. Continental Shelf Research, 31, 23-36,doi:10.1016/j.csr.2010.10.014.

Nittrouer, C., Raubenheimer, B., Wheatcroft, R., Lessons learned from comparison of mesotidal sand- and mudflats, Continental Shelf Research, this special issue.

Nowacki, D., Ogston, A., Water-surface elevation control on channel to flat transfer of sediment on intertidal flats, Continental Shelf Res., in review for special issue.

Ozdemir, C. E., Hsu, T.-J., Balachandar, S., 2010. A numerical investigation of fine particle laden flow in oscillatory channel: the role of particle-induced density stratification, *J. Fluid Mech., 665, 1-45.*

Postma, H., 1961. Transport and accumulation of suspended matter in the Dutch Wadden Sea. Neth. J. Sea Res., 1, 148–180, doi:10.1016/0077-7579(61)90004-7.

Pritchard, D., Hogg, A. J., Roberts, W., 2002. Morphological modeling of intertidal mudflats: the role of cross-shore tidal currents, Cont. Shelf Res., 22, 1887-1895.

Pritchard, D., and Hogg, A. J., 2003. Cross-shore sediment transport and the equilibrium morphology of mudflats under tidal currents, J. Geophys. Res., 108 (C10), 3313.

Ralston, D. K., Stacey, M. T., 2007. Tidal and meteorological forcing of sediment transport in tributary mudflat channels, Cont. Shelf Res., 27, 1510-1527.

Ralston, D. K., Geyer, W. R., Lerczak A. J., 2010. Structure, variability, and salt flux in a strongly forced salt wedge estuary, J. Geophys. Res., 115, C06005, doi:10.1029/2009JC005806

Ralston, D., P. Traykovski, and R. Geyer, Estuarine dynamics and sediment transport on the Skagit tidal flats. in review for special issue.

Ridderinkhof, H., van der Ham, R., van der Lee, W., 2000. Temporal variations in concentration and transport of suspended sediments in a channel-flat system in EMS-Dollard estuary. Cont. Shelf Res., 1479-1493.

Roberts, W., Le Hir, P. and Whitehouse, R. J. S., 2000. Investigation using simple mathematical models of the effect of tidal currents and waves on the profile shape of intertidal mudflats. *Cont. Shelf Res.*, 20, 1079-1097.

Sanford, L. P., Maa, J. P.-Y., 2001. A unified erosion formulation for fine sediments, Mar. Geol., 179, 9 – 23, doi:10.1016/S0025-3227(01)00201-8.

Shchepetkin, A. F., McWilliams, J. C., 1998. Quasi-monotone advection schemes based on explicit locally adaptive dissipation. *Monthly Weather Review*, **126,** 1541-1580.

Shchepetkin, A. F., McWilliams, J. C., 2005. The region oceanic modeling system (ROMS): a split-explicit, free-surface, topography-following-coordinate oceanic model. *Ocean Modeling*, 9, 347-404.

Shigematsu, T., Liu, P. L. F., Oda, K., 2004. Numerical modeling of the initial stages of dam-break waves. Journal of Hydraulic Research; 42(2): 183-195.

Son, M., and T.-J. Hsu 2011a. The effects of flocculation and bed erodibility on modeling cohesive sediment resuspension. J. Geophys. Res., 116, C03021, doi:10.1029/2010JC006352.

Son, M., Hsu, T.-J., 2011b. Idealized study on cohesive sediment flux by tidal asymmetry, *Environmental Fluid Mechanics*, 11(2), 183-201, DOI 10.1007/s10652-010-9193-9.

Stevens, A. W., Wheatcroft, R. A., Wiberg, P. L., 2007. Seabed properties and sediment erodibility along the western Adriatic margin, Italy. Cont. Shelf Res., 27, 400– 416, doi:10.1016/j.csr.2005.09.009.

de Swart H. E., Zimmerman, J. T. F., 2009. Morphodynamics of Tidal Inlet Systems. Annu. Rev. Fluid Mech., 41:203–29.

Torres-Freyermuth, A., Hsu, T.-J., 2010. On the dynamics of wave-mud interaction: a numerical study. *Journal of Geophysical Research*, 115, C07014, doi:10.1029/2009JC005552.

Uncles R. J., Jordan, M. B., 1980. Aone-dimensional representation of residual currents in the Severn estuary and associated observations. Estuar. Coast. Mar. Sci., 10:39–60.

van Straaten, J. M. J. U., Keunen, P. H., 1958. Tidal action as a cause of clay accumulation. J. Sediment. Petrol., 28, 406–413.

Warner, J. C., Geyer, W. R., Lerczak, J. A., 2005. Numerical modeling of an estuary: A comprehensive skill assessment. J. Geophys. Res., 110, C05001, doi:10.1029/2004JC002691.

Warner, J. C., Sherwood, C. R., Signell, R. P., Harris, C. K., Arango, H. G., 2008a. Development of a three-dimensional, regional, coupled wave, current, and sediment-transport model. Computer & Geosciences, 34, 1284-1306.

Warner, J. C., Butman, B., Dalyander, S., 2008b. Storm-driven sediment transport in Massachusetts Bay. Cont. Shelf Res., (28), 257-282.

Wiberg P., Wheatcroft, R., Hill, P., Milligan, T., Law, B., Newgard, J., Sediment erodibility on a tidal flat: channel complexes in southern Willapa Bay, Continental Shelf Res., in review for special issue.

Winterwerp, J. C., A. J. Manning, C. Martens, T. de Mulder, and J. van Lede 2006. A heuristic formula for turbulence-induced flocculation of cohesive sediment. Estuarine, Coastal Shelf Sci., 68, 195–207, doi:10.1016/j.ecss.2006.02.003.

Zhang, Q., Liu, P. L.-F., 2008. A numerical study of swash flow generated by bores. Coastal Eng., 55, 1113-1134.

Table:

Table 1: Summary of all model runs investigated in this study

Case No.	Settling velocity W_s	Crit. stress τ_b	Additional comments
Case 1	0.5 (mm/s)	0.15 (Pa)	
Case 2	0.5 (mm/s)	0.15 (Pa)	Case 1 without sediment-induced density stratification
Case 3	0.25 (mm/s)	0.15 (Pa)	Lower settling velocity
Case 4	1.0 (mm/s)	0.15 (Pa)	Higher settling velocity
Case 5	0.5 (mm/s)	0.13 (Pa)	Lower critical shear stress
Case 6	0.5 (mm/s)	0.15 (Pa)	Case 1 but with limited erosion

Figure Caption:

Figure 1: Idealized tidal flat used for the present numerical study. The red-plus symbols represent the location of numerical sensors. A local coordinate z_b is defined to represent the distance from the bed at a specific cross-shore location. The blue line represents the water-surface elevation at low (solid) and high (dashed) tides.

Figure 2: (a) A snapshot of the velocity field and suspended-sediment concentration during flood (at t=2.5 hr of the third tidal cycle) for Case 1 calculated using the RANS-VOF model. (b) The

corresponding cross-shore distribution of streamwise velocity at the first grid point (2.5 cm) above the bed (blue-dashed curve) and depth-averaged sediment concentration (red-solid curve).

Figure 3: (a) A snapshot of the velocity field and suspended-sediment concentration during ebb (at t=9.6 hr of the third tidal cycle) for Case 1 calculated using the RANS-VOF model. (b) Cross-shore distribution of streamwise velocity at the first grid point (2.5 cm) above the bed (blue-dashed curve) and depth-averaged sediment concentration (red-solid curve). This instant is chosen as the time when the ebb tidal edge passes the same location as that shown for flood tidal edge in Figure 1.

Figure 4: RANS-VOF model results showing the cross-shore distribution of depth-averaged flow velocity throughout the tidal cycle (every 20 minute, or T/36 interval, black lines) for Case 1. The envelope of the numerical model results can be compared with maximum tidal velocity magnitude predicted by FA96 theory (red-dashed curves).

Figure 5: Time series at the landward end of the lower flat (x=1208 m) for Case 1 simulated by the RANS-VOF model for (a) sediment concentration and (b) bottom stress where the red-dashed line represents τ_b=0.15 Pa. Vertical profiles of velocity (c1), sediment concentration (c2) and turbulence intensity (c3) during flood (solid-black) and ebb (red-dashed). The timing of the profiles shown in (c1-c3) is marked with the blue dashed lines in (b). The blue-dotted curves near the velocity profiles in (c1) are the corresponding logarithmic-law velocities reconstructed with the same roughness and friction velocity as in the numerical model.

Figure 6: Time series at the subtidal region (x=-92 m) for Case 1 simulated by the RANS-VOF model for (a) sediment concentration and (b) bottom stress where the red-dashed line represents τ_b=0.15 Pa. Vertical profiles of velocity (c1), sediment concentration (c2) and turbulence intensity (c3) during flood (solid-black) and ebb (red-dashed). The timing of the profiles shown in (c1-c3) is marked with the blue dashed lines in (b). The blue-dotted curves near the velocity profiles in (c1) are the corresponding logarithmic-law velocities reconstructed with the same roughness and friction velocity as in the numerical model.

Figure 7: ROMS estimate of the cross-shore depth-averaged flow velocity for Case 1, using a critical depth of (a) h_{crit}=10 cm, and (b) h_{crit}=2 cm. The results in (b) are similar to RANS-VOF model results and consistent with FA96 theory when very small critical depth is used. However, when the commonly used value of h_{crit}=10 cm is used (a), the depth-averaged velocity is under-predicted both during flood and ebb.

Figure 8: Time series from ROMS of the turbid tidal edge located at the seaward end of the lower flat similar to that predicted by RANS-VOF (Case1, see Figure 5). (a) sediment concentration (h_{crit}=2.0 cm) and (b) bottom stress. Black and gray lines in (b) are for h_{cirt} of 2.0 and 10 cm, respectively.

Figure 9: RANS-VOF model results showing vertical profiles of velocity (a1, b1), sediment concentration (a2, b2) and turbulence intensity (a3, b3) during early flood (t=2.78 hr; a1~a3) and mid flood (t=3.89 hr; b1~b3) at x=1208 m. The red-dashed curves represent results without considering the sediment-induced density stratification terms in the k and ε equations. In (a1)

and (b1), the black dash-dotted (red dotted) curves represent the logarithmic law using the bottom stress obtained from numerical-model results with (without) the consideration of sediment-induced density stratification. Note the different concentration scales between (a2) and (b2).

Figure 10: RANS-VOF model results of time series of sediment concentration at the mid-flat (see (a), x=1208 m) and the lower flat (see (b), x=-692 m) for Case 3.

Figure 11: Tidally averaged and depth-integrated landward (positive) and seaward (negative) sediment-transport rate for Case 1 (W_s= 0.5 mm/s, squares), Case 3 (W_s= 0.25 mm/s, crosses) and Case 4 (W_s= 1 mm/s, circles) computed with the RANS-VOF model. Positive values indicate landward transport.

Figure 12: Tidally averaged and depth-integrated landward (positive) and seaward (negative) sediment-transport rate calculated with ROMS using h_{crit}=2 cm (black curve) and h_{crit}=10 cm (gray curve).

Figure 13: Tidally averaged and depth-integrated landward (positive) and seaward (negative) sediment-transport rate for Case 1 (squares, τ_b=0.15 Pa), Case 5 (circles, τ_b=0.13 Pa) and Case 6 (∇ symbols, limited erosion of 0.03 kg/m^2) computed with the RANS-VOF model.

Figure 14: Example of time-series data collected in a channel (left panels) and on the nearby flat surface (right panels) in Willapa Bay on 23 July 2009 showing (a1, b1) profiles of velocity, (a2, b2) uncalibrated backscatter as a proxy for suspended sediment concentration, and (a3, b3) estimated bed stress using the logarithmic law. In (a) and (b) the solid line indicates the water

surface and the dashed line indicates the limit of reliable profile data. The grey boxes in (c) indicate times when sensors were out of the water.

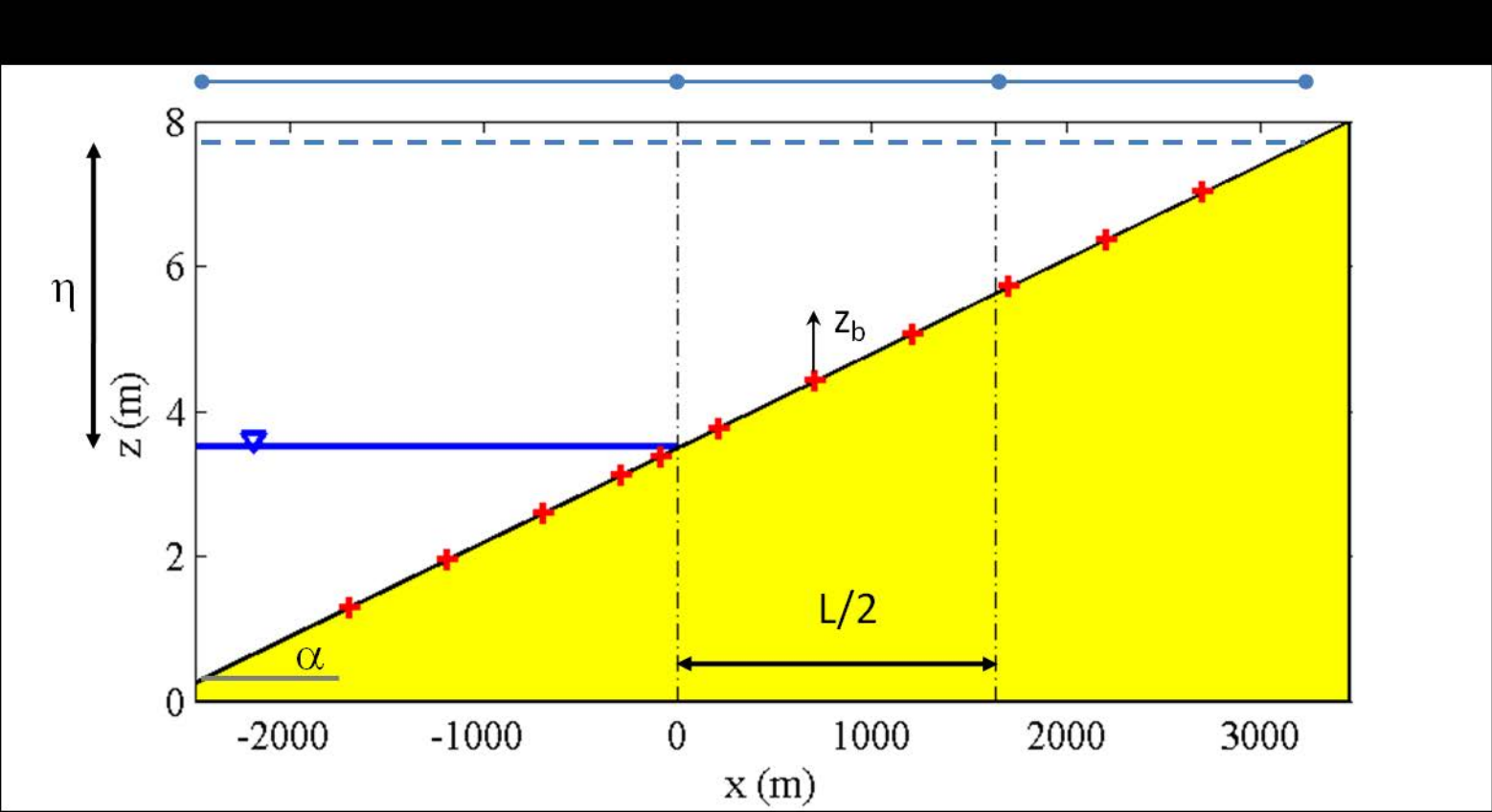
η
z (m)
8
6
4
2
0
z_b
L/2
α
-2000
-1000
0
1000
2000
3000
x (m)

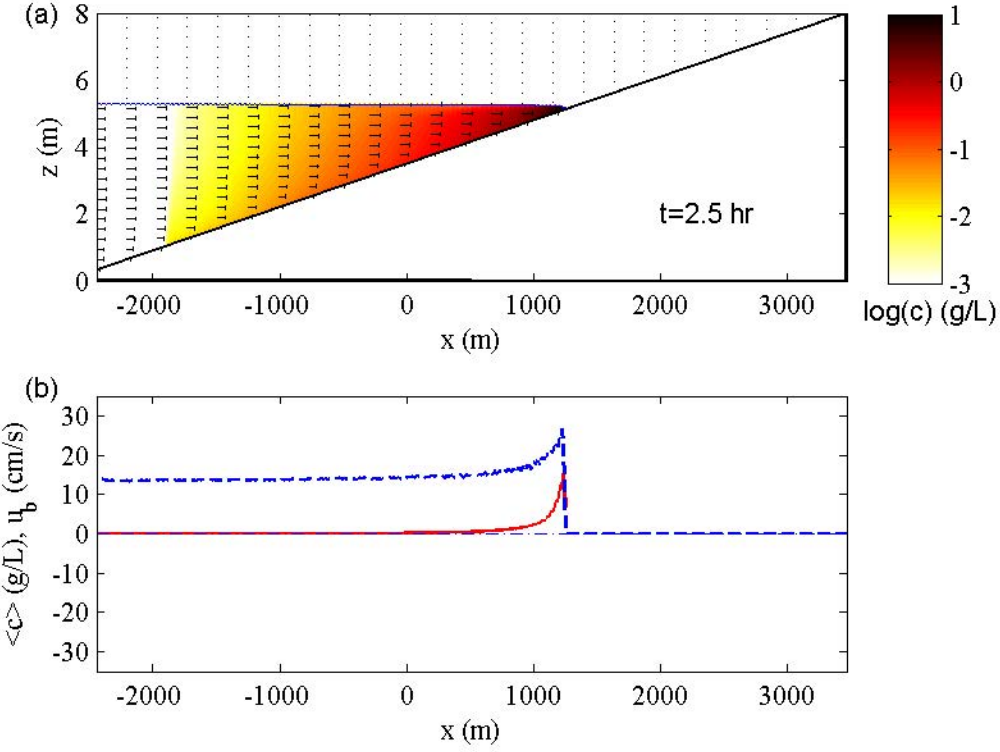
(a)
z (m)
x (m)
t=2.5 hr
log(c) (g/L)
(b)
<c> (g/L), u_b (cm/s)
x (m)

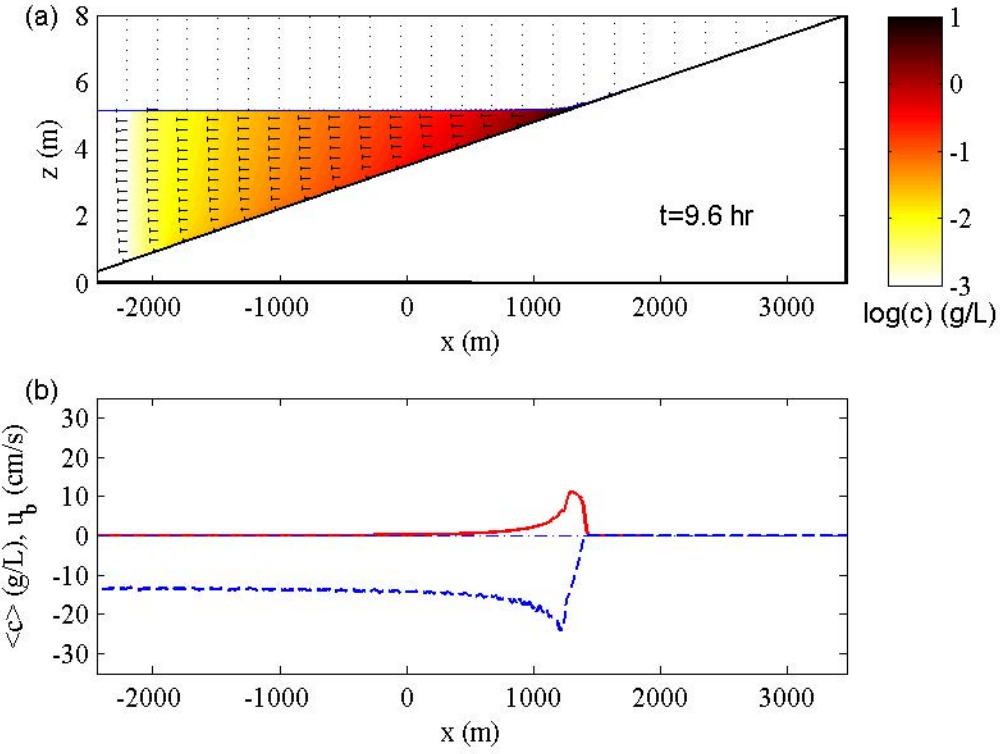
(a)
z (m)
x (m)
t=9.6 hr
log(c) (g/L)
(b)
<c> (g/L), u_b (cm/s)
x (m)

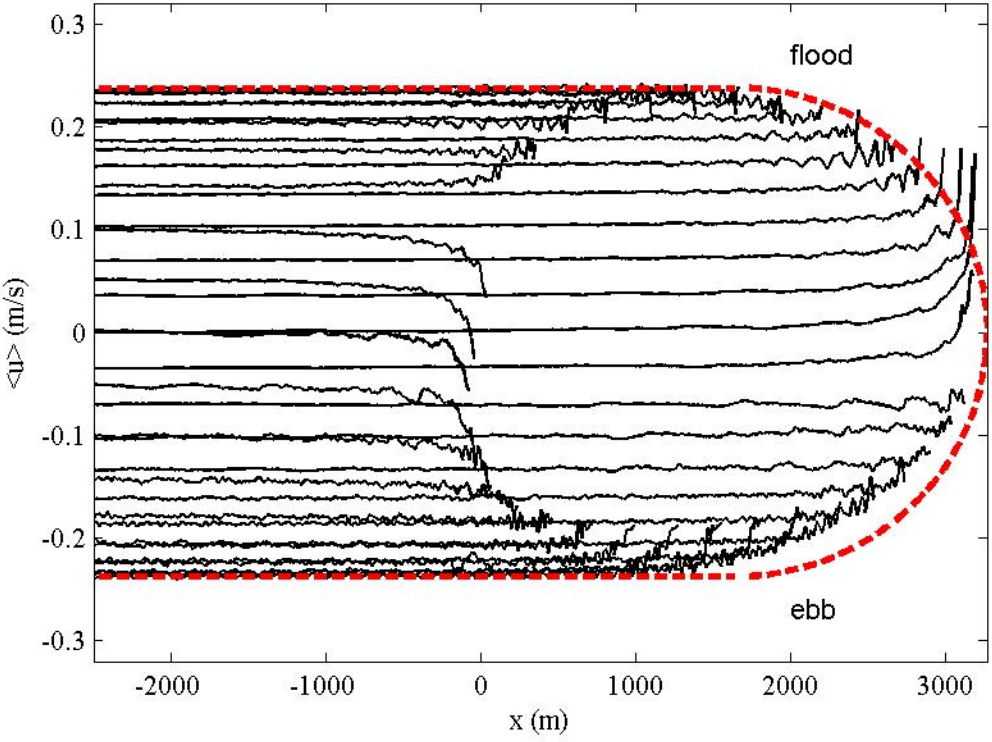
flood
ebb
<u> (m/s)
x (m)
0.3
0.2
0.1
0
-0.1
-0.2
-0.3
-2000
-1000
0
1000
2000
3000

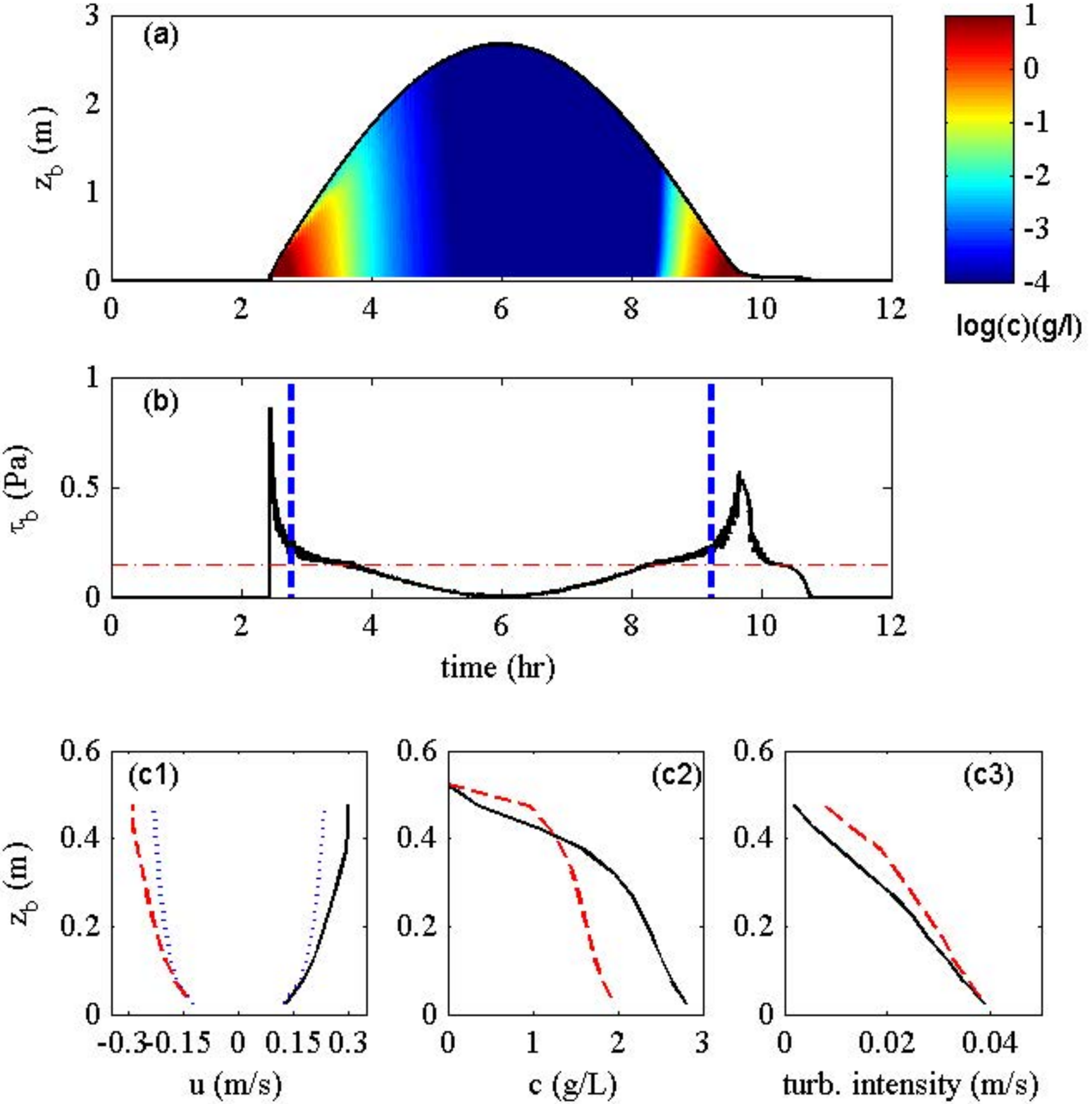
(a)
z_b (m)
log(c)(g/l)
(b)
τ_b (Pa)
time (hr)
(c1)
(c2)
(c3)
z_b (m)
u (m/s)
c (g/L)
turb. intensity (m/s)

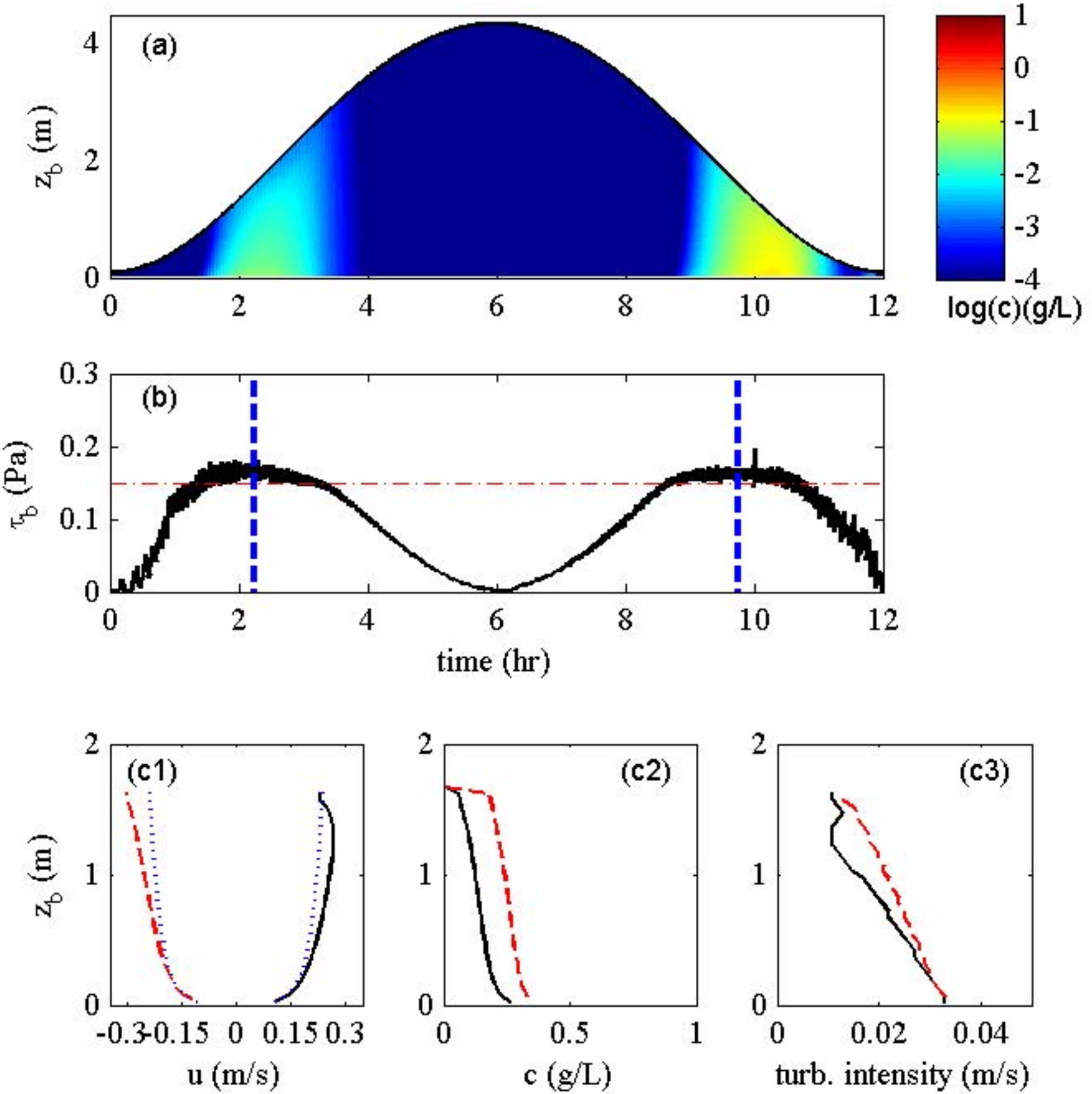
(a)
z_b (m)
0
2
4
0
2
4
6
8
10
12
1
0
-1
-2
-3
-4
log(c)(g/L)
(b)
τ_b (Pa)
0
0.1
0.2
0.3
time (hr)
(c1)
(c2)
(c3)
z_b (m)
-0.3
-0.15
0
0.15
0.3
u (m/s)
0.5
1
c (g/L)
0.02
0.04
turb. intensity (m/s)

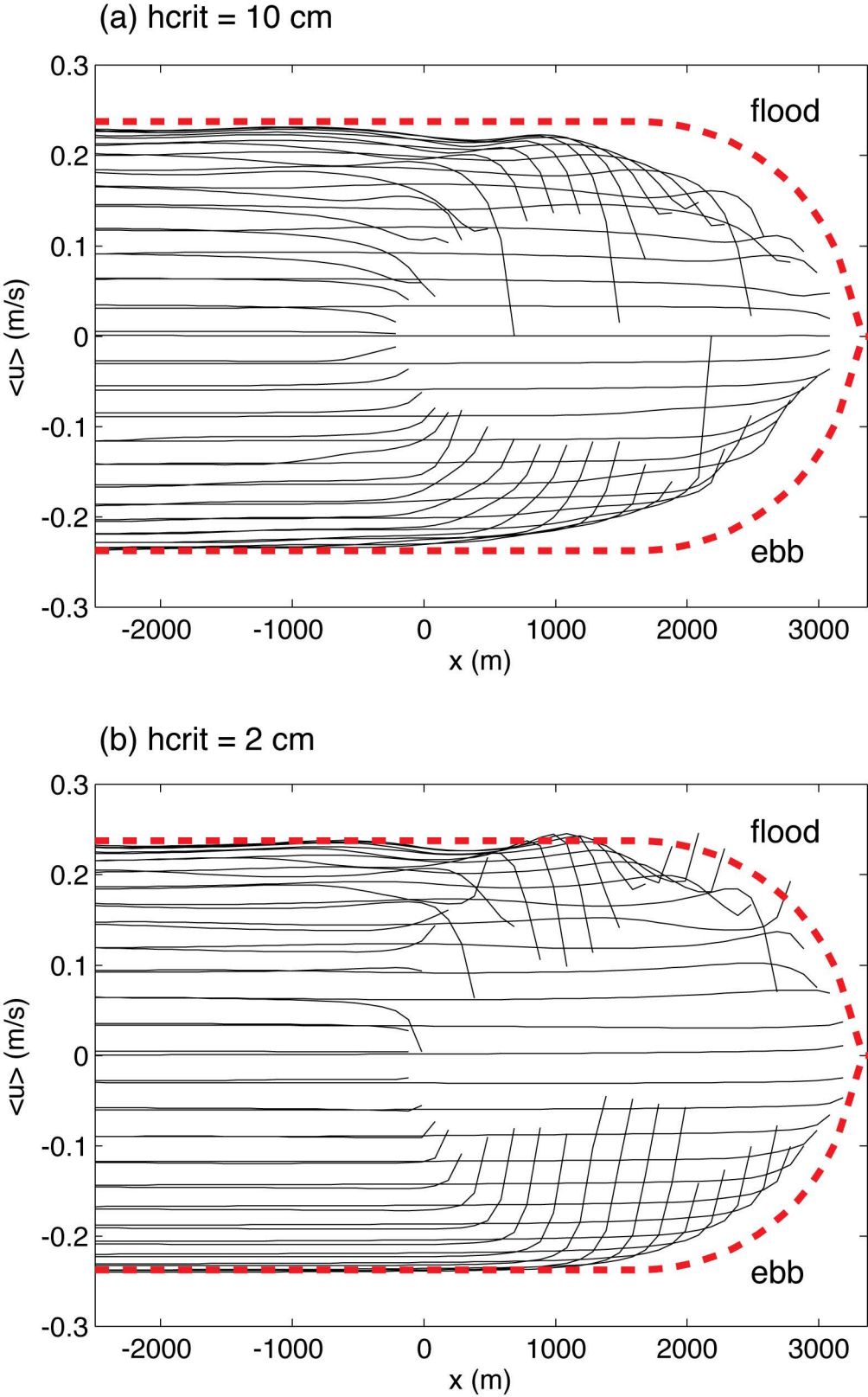
(a) hcrit = 10 cm
flood
ebb
<u> (m/s)
x (m)
0.3
0.2
0.1
0
-0.1
-0.2
-0.3
-2000
-1000
0
1000
2000
3000
(b) hcrit = 2 cm
flood
ebb
<u> (m/s)
x (m)

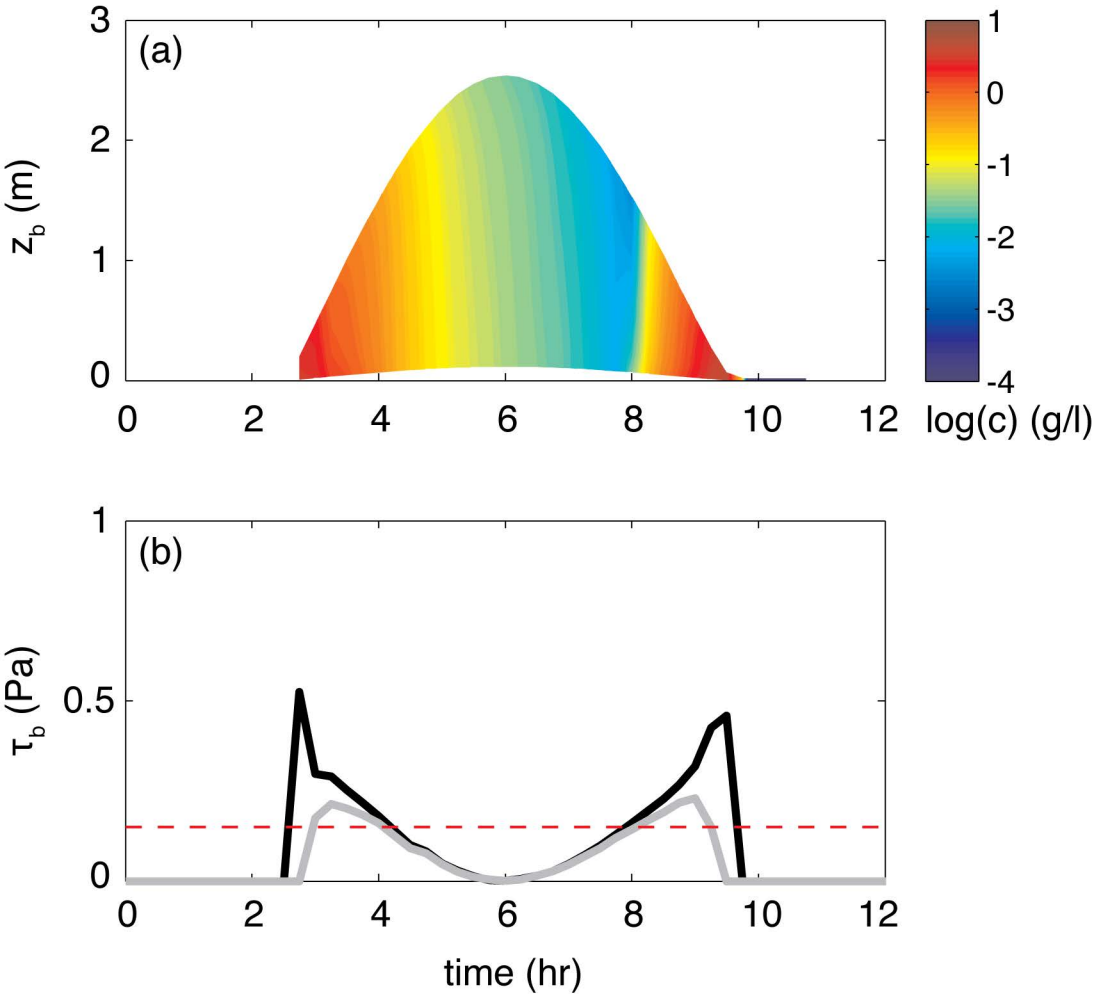
(a)
z_b (m)
3
2
1
0
0
2
4
6
8
10
12
1
0
-1
-2
-3
-4
log(c) (g/l)
(b)
τ_b (Pa)
1
0.5
0
0
2
4
6
8
10
12
time (hr)

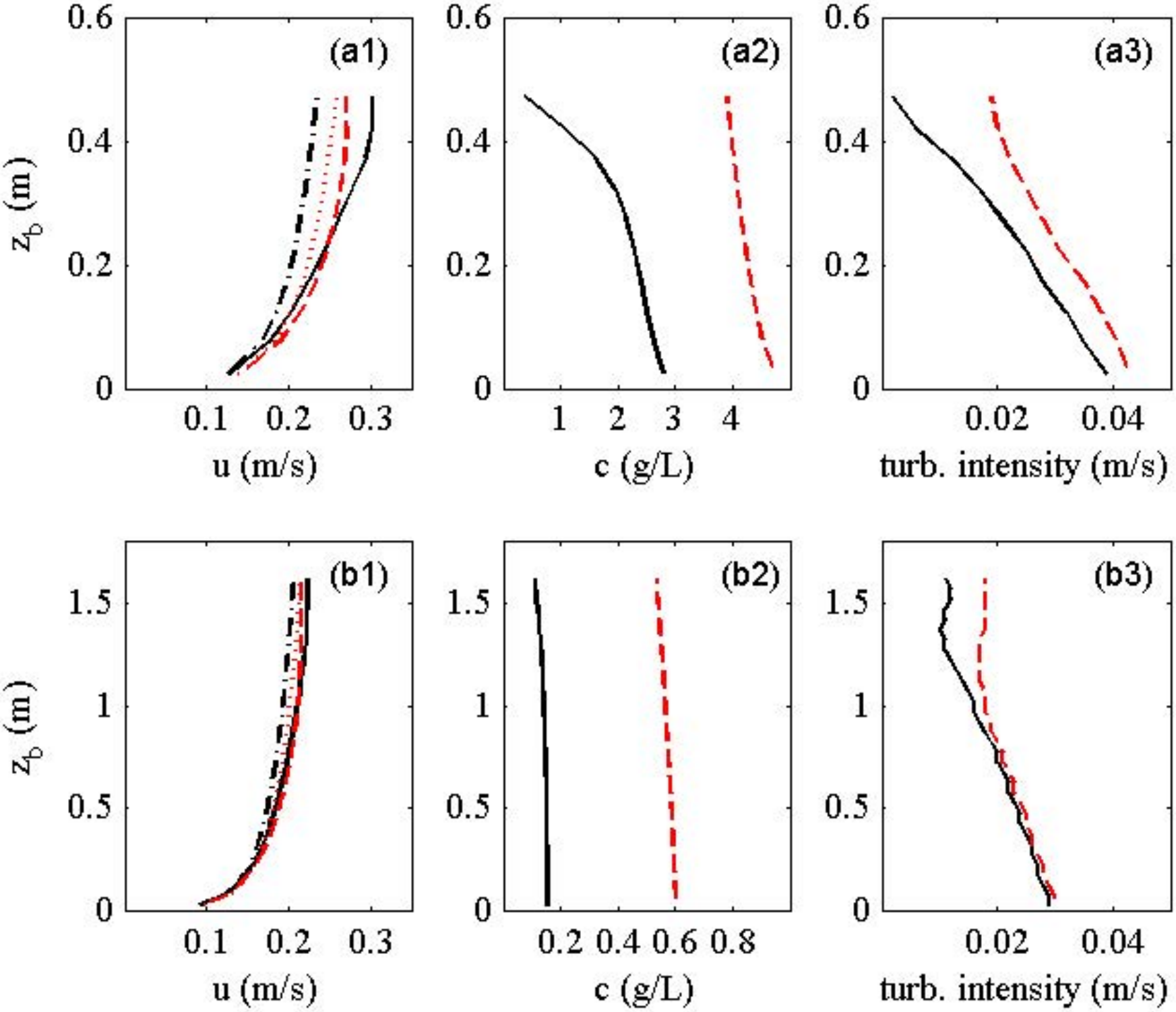
(a1)
(a2)
(a3)
(b1)
(b2)
(b3)
z_b (m)
u (m/s)
c (g/L)
turb. intensity (m/s)
0.6
0.4
0.2
0
1.5
1
0.5
0.1
0.2
0.3
1
2
3
4
0.02
0.04
0.2
0.4
0.6
0.8

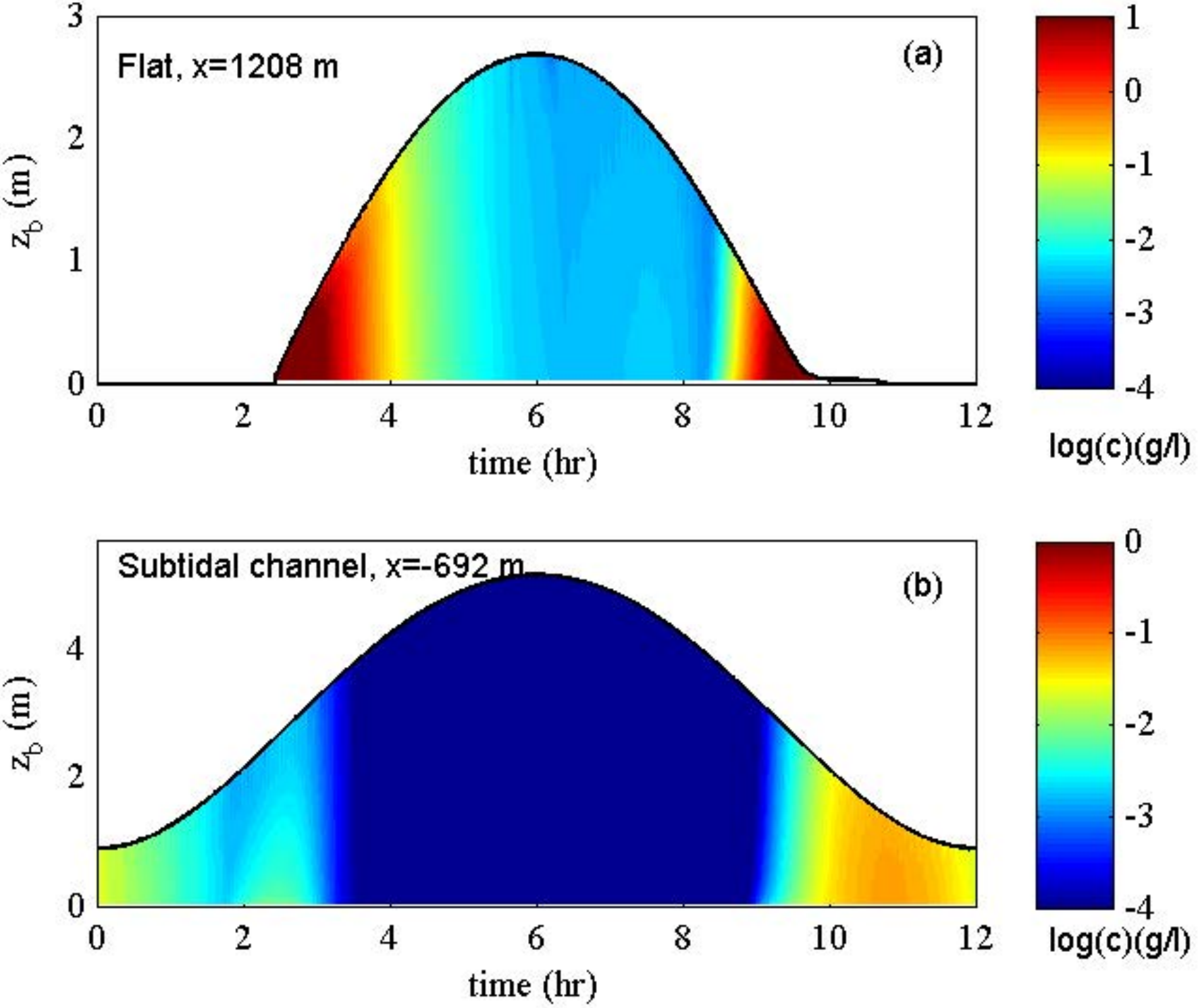
Flat, x=1208 m
(a)
z_b (m)
time (hr)
log(c)(g/l)
Subtidal channel, x=-692 m
(b)
z_b (m)
time (hr)
log(c)(g/l)

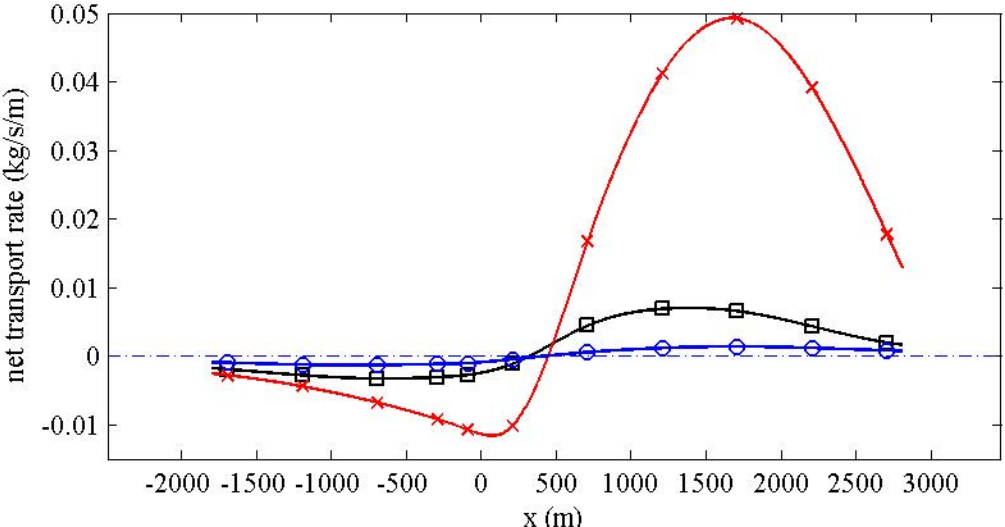
0.05
0.04
0.03
0.02
0.01
0
-0.01
net transport rate (kg/s/m)
-2000 -1500 -1000 -500 0 500 1000 1500 2000 2500 3000
x (m)

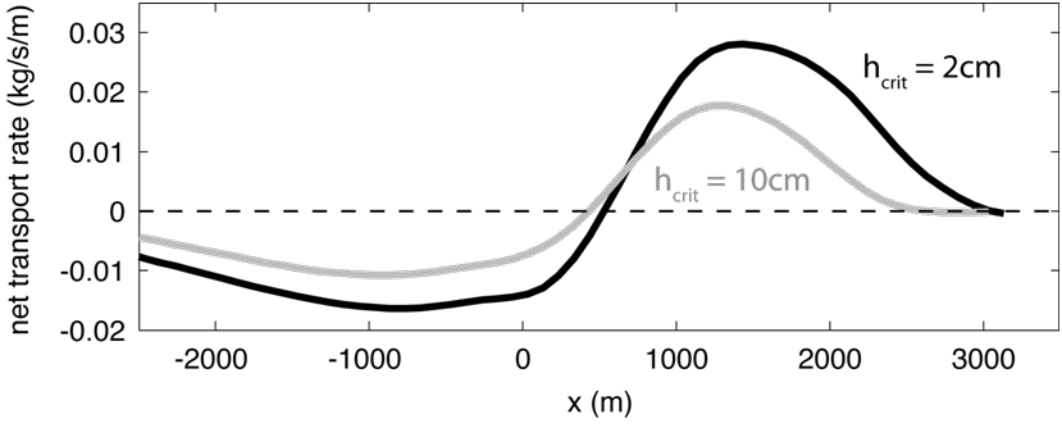
net transport rate (kg/s/m)
0.03
0.02
0.01
0
-0.01
-0.02
-2000
-1000
0
1000
2000
3000
x (m)
h crit = 2cm
h crit = 10cm

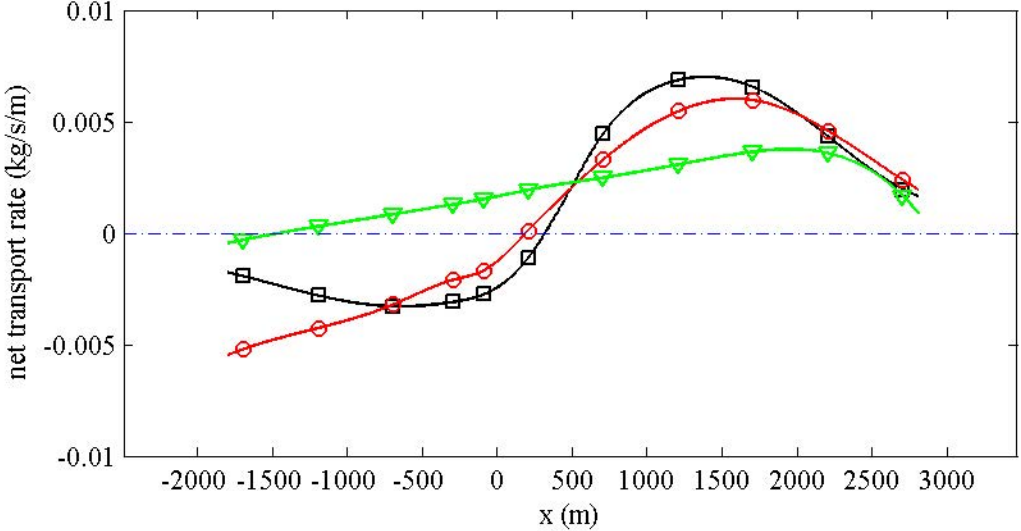
0.01
0.005
0
-0.005
-0.01
net transport rate (kg/s/m)
-2000 -1500 -1000 -500 0 500 1000 1500 2000 2500 3000
x (m)

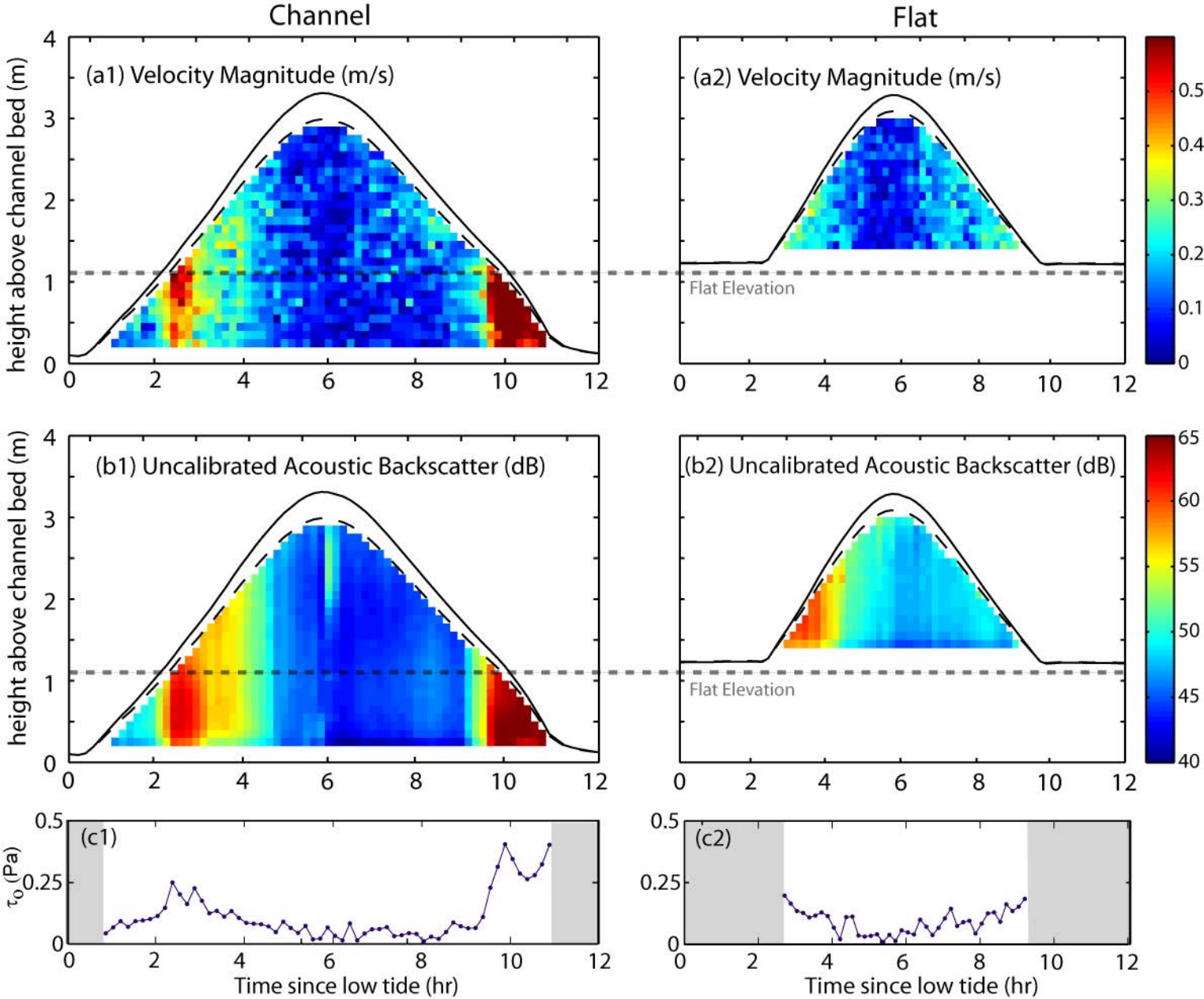
Channel
Flat
(a1) Velocity Magnitude (m/s)
(a2) Velocity Magnitude (m/s)
Flat Elevation
(b1) Uncalibrated Acoustic Backscatter (dB)
(b2) Uncalibrated Acoustic Backscatter (dB)
Flat Elevation
height above channel bed (m)
(c1)
(c2)
τ0 (Pa)
Time since low tide (hr)
Time since low tide (hr)